Apportionment of the Pre-Industrial to Present-Day Climate Forcing by Methane Using UKESM1: The Role of the Cloud Radiative Effect

Fiona M O'connor, Ben T Johnson, Omar Jamil, Timothy Andrews, Jane P Mulcahy, James Manners

AGU ADVANCING EARTH AND SPACE SCIENCE

JAMES | Journal of Advances in Modeling Earth Systems®

RESEARCH ARTICLE
10.1029/2022MS002991

Key Points:

- The direct radiative effect of methane in UKESM1 is consistent with line-by-line radiative transfer calculations
- The total methane effective radiative forcing (ERF) in UKESM1 includes an aerosol-mediated cloud forcing due to changes in cloud activation
- The ERF also includes a dynamically driven cloud forcing from tropospheric warming and a reduction in cloud fraction

Correspondence to:
F. M. O'Connor,
fiona.oconnor@metoffice.gov.uk

Citation:
O'Connor, F. M., Johnson, B. T., Jamil, O., Andrews, T., Mulcahy, J. P., & Manners, J. (2022). Apportionment of the pre-industrial to present-day climate forcing by methane using UKESM1: The role of the cloud radiative effect. *Journal of Advances in Modeling Earth Systems*, *14*, e2022MS002991. https://doi.org/10.1029/2022MS002991

Received 17 JAN 2022
Accepted 26 AUG 2022

Author Contributions:
Conceptualization: Fiona M. O'Connor, Ben T. Johnson
Data curation: Ben T. Johnson
Formal analysis: Fiona M. O'Connor, Ben T. Johnson, Timothy Andrews
Investigation: Fiona M. O'Connor, Ben T. Johnson
Methodology: Fiona M. O'Connor, Ben T. Johnson, Omar Jamil
Software: Fiona M. O'Connor, Ben T. Johnson, Omar Jamil, James Manners
Validation: Jane P. Mulcahy
Visualization: Fiona M. O'Connor, Ben T. Johnson

Apportionment of the Pre-Industrial to Present-Day Climate Forcing by Methane Using UKESM1: The Role of the Cloud Radiative Effect

Fiona M. O'Connor[1,2], Ben T. Johnson[1], Omar Jamil[3], Timothy Andrews[1], Jane P. Mulcahy[1], and James Manners[4]

[1]Met Office Hadley Centre, Exeter, UK, [2]Department of Mathematics and Statistics, Global Systems Institute, University of Exeter, Exeter, UK, [3]Institute of Data Science and Artificial Intelligence, University of Exeter, Exeter, UK, [4]Met Office, Exeter, UK

Abstract The Year 1850 to 2014 increase in methane from 808 to 1831 ppb leads to an effective radiative forcing (ERF) of 0.97 ± 0.04 W m^{-2} in the United Kingdom's Earth System Model, UKESM1. The direct methane contribution is 0.54 ± 0.04 W m^{-2}. It is better represented in UKESM1 than in its predecessor model HadGEM2 due to shortwave and longwave absorption improvements and the absence of an anomalous dust response in the UKESM1 simulations. An indirect ozone ERF of 0.13–0.20 W m^{-2} is due to the tropospheric ozone increase outweighing that of the stratospheric decrease. The indirect water vapor ERF of 0.02–0.07 W m^{-2} is consistent with previous estimates. The methane increase also leads to a cloud radiative effect of 0.12 ± 0.02 W m^{-2} from thermodynamic adjustments and aerosol-cloud interactions (aci). Shortwave and longwave contributions of 0.23 and −0.35 W m^{-2} to the cloud forcing arise from radiative heating and stabilization of the upper troposphere, reducing convection and global cloud cover. The aerosol-mediated contribution (0.28–0.30 W m^{-2}) is due to changes in oxidants reducing new particle formation (−8%), shifting the aerosol size distribution toward fewer but larger particles. Cloud droplet number concentration decreases and cloud droplet effective radius increases. This reduction in the Twomey effect switches the cloud forcing sign (−0.14 to 0.12 W m^{-2}) and is due to chemistry-aerosol-cloud coupling in UKESM1. Despite uncertainties in rapid adjustments and process representation in models, these results highlight the potential importance of chemistry-aerosol-cloud interactions and dynamical adjustments in climate forcing.

Plain Language Summary Methane is the second most important greenhouse gas after carbon dioxide. Methane is also chemically reactive in the atmosphere, and can cause changes in ozone, which is also a greenhouse gas. Methane can also affect the amount of water vapor (WV) in the atmosphere, where it too acts as a greenhouse gas. Aerosols, formed in the atmosphere through chemical processing, are also affected by methane. This study quantifies the impact of changes in methane concentration since the pre-industrial period on the Earth's energy budget at the present day and examines the impact from methane itself, as well as the impact from the additional methane-driven changes in ozone, WV, aerosols, and clouds. The biggest impact (~55%) is from methane itself, and of the remaining impact on the Earth's energy budget from methane, most can be attributed to ozone and clouds. The contribution from clouds is partly driven by changes in aerosol properties and partly driven by heating and a reduction in cloud cover. The impact from WV is small and is consistent with previous estimates. This study highlights the potential importance of including chemistry-aerosol-cloud interactions when quantifying the effect of pre-industrial to present-day changes in atmospheric constituents on climate.

1. Introduction

Methane (CH_4) is the second most important greenhouse gas (GHG) after carbon dioxide (CO_2) (Myhre et al., 2013). Due to its relatively short atmospheric lifetime of 11.2 ± 1.3 years (Prather et al., 2012) and its radiative efficiency being an order of magnitude larger than for CO_2 (Myhre et al., 2013; Ramaswamy et al., 2001), CH_4 has an important role in mitigating near-term climate change (e.g., Abernethy et al., 2021; Allen et al., 2018; Allen et al., 2021; UNEP, 2011; UNEP, 2021). However, future concentrations may be subject to climate feedbacks involving CH_4 natural sources (e.g., Dean et al., 2018; Gedney et al., 2019; Kleinen et al., 2021; O'Connor

Writing – original draft: Fiona M. O'Connor
Writing – review & editing: Fiona M. O'Connor, Ben T. Johnson, Omar Jamil, Timothy Andrews, Jane P. Mulcahy, James Manners

et al., 2010; Thornhill, Collins, Olivié, et al., 2021). It is therefore important to quantify its climate forcing and relevant feedbacks for understanding the historical and future evolution of climate.

In relation to its climate forcing, CH_4 has a direct radiative effect and indirect effects due to its reactivity. As well as being a tropospheric ozone (O_3) precursor, CH_4 affects stratospheric O_3 (Pawson et al., 2014) and together, the O_3 changes lead to an indirect contribution to the total CH_4 forcing. CH_4 oxidation is also a major sink for the hydroxyl (OH) radical, and changes in CH_4 lead to changes in O_3, OH, and other oxidants. These oxidants determine the rate of formation of secondary aerosol such as sulfate and secondary organic aerosol (e.g., Kelly et al., 2018; Mulcahy et al., 2020), potentially giving rise to additional indirect effects (e.g., Karset et al., 2018; Shindell et al., 2009) through aerosol-radiation interactions (ari) and/or aerosol-cloud interactions (aci), although these effects have not been well quantified to date.

Water vapor (WV) is also an important component of the radiative balance in the stratosphere (e.g., Forster & Shine, 1999). Trends in observed stratospheric WV could be due to increases in stratospheric CH_4 oxidation (Hansen et al., 2005) or direct aircraft emissions (Wilcox et al., 2012). However, some of the observed increase can be attributed to a climate feedback (e.g., Dessler et al., 2013). Studies disagree on the relative role of CH_4 (e.g., Hurst et al., 2011; Oman et al., 2011). Nevertheless, it is clear that indirect forcings through changes in O_3, stratospheric WV, and potentially aerosols, can significantly impact CH_4 forcing (Hansen et al., 2005; Myhre et al., 2013; Shindell et al., 2005, 2009; Thornhill, Collins, Kramer, et al., 2021; Winterstein et al., 2019).

Recent studies that rank anthropogenic drivers of climate change make use of the effective radiative forcing (ERF) as the preferred metric of choice (e.g., O'Connor et al., 2021; Smith et al., 2018; Smith et al., 2020; Thornhill, Collins, Kramer, et al., 2021) since it is more representative of the predicted global mean temperature response (Hansen et al., 2005; Richardson et al., 2019). It was defined in the Intergovernmental Panel on Climate Change (IPCC) 5th assessment report (AR5; Myhre et al., 2013) at the top-of-atmosphere (TOA) as:

$$\mathrm{ERF} = \mathrm{IRF} + \sum_{i=1}^{n} A_i \tag{1}$$

where IRF is the TOA instantaneous radiative forcing (IRF) from an imposed perturbation (e.g., a change in a GHG concentration) and A_i is a rapid atmospheric or land surface adjustment (e.g., atmospheric temperature, clouds, water vapor, albedo, etc.) that gives rise to additional positive or negative changes in the net TOA radiative fluxes. The ERF differs from the more traditional radiative forcing metric, in that the latter only includes a stratospheric temperature adjustment, whereas the ERF also includes tropospheric and land surface adjustments.

In the case of the direct radiative effect of CH_4, Smith et al. (2018) found that the present-day (PD) CH_4 ERF is approximately equivalent to its IRF. The rapid adjustment associated with stratospheric temperature is negligible and the other adjustments (e.g., tropospheric temperature and water vapor (WV)) are small, have opposing signs, and roughly sum to zero. However, as indicated above, there are additional Earth System (ES) interactions or chemical adjustments that affect the net TOA radiative fluxes when CH_4 is considered within a full ES context (e.g., Hansen et al., 2005; Shindell et al., 2005, 2009; Winterstein et al., 2019). Therefore, when quantifying the climate forcing of CH_4, ES interactions or chemical adjustments need to be fully considered (Myhre et al., 2013; Shindell et al., 2009) in addition to physical adjustments (Smith et al., 2018).

A recent study by Thornhill, Collins, Kramer, et al. (2021) quantified a range of PD anthropogenic ERFs and considered both physical and chemical adjustments using an ensemble of models that participated in the Aerosol and Chemistry Model Intercomparison Project (AerChemMIP; Collins et al., 2017). The multi-model PD CH_4 ERF was 0.67 ± 0.17 W m^{-2}. Some of the model spread is due to differing complexities in the representation of chemistry in the respective models (and hence differences in their indirect contributions, e.g., from O_3). However, some of the model diversity is due to differences in the sign and magnitude of the cloud adjustment (-0.06 to 0.24 W m^{-2}). Although other AerChemMIP models show a positive cloud adjustment (e.g., GISS-E2-1 (Bauer et al., 2020) and CESM-WACCM (Emmons et al., 2020)), the United Kingdom's ES Model, UKESM1 (Sellar et al., 2019), has the largest positive cloud adjustment of the AerChemMIP models. This results in UKESM1 being one of only two models (including CESM-WACCM) to have a positive tropospheric adjustment overall and the highest PD CH_4 ERF of 0.97 ± 0.04 W m^{-2} (O'Connor et al., 2021) of the multi-model ensemble.

In the Thornhill, Collins, Kramer, et al. (2021) study, radiative kernels (Chung & Soden, 2015; Smith et al., 2018, 2020) and diagnostic radiation calls (Ghan, 2013) enabled a breakdown of the total CH_4 ERF into different constituents (gas phase vs. aerosol phase). However, it is unclear whether the relevant adjustments are additive when more than one forcing agent is perturbed (as is the case for CH_4 in an ES context). The kernel approach also cannot distinguish between cloud adjustments that are dynamically driven and those that are due to changes in aerosol-mediated cloud nucleation (Thornhill, Collins, Kramer, et al., 2021). As a result, a complete process-based understanding of the UKESM1 total CH_4 ERF and the AerChemMIP multi-model diversity in the PD CH_4 ERF is lacking.

The aim of the current study is thus to apportion the UKESM1 PD CH_4 forcing quantified in O'Connor et al. (2021) between the direct CH_4 contribution and indirect contributions. This study will also aim to test whether the relevant contributions (including adjustments) are additive and provide a process-based understanding of the positive cloud adjustment in UKESM1. Although CH_4 can affect the lifetime of other GHGs such as chlorofluorocarbons (Boucher et al., 2009) or nitrous oxide (Hsu & Prather, 2010), they are concentration-driven in UKESM1 and their response to CH_4 is therefore not included. As a result, the focus here will be on the direct CH_4 ERF from the change in CH_4 concentration between the pre-industrial (PI) period and the PD, and the corresponding indirect ERFs from CH_4-driven changes in O_3, stratospheric WV, clouds, and potentially aerosols. The paper is organized as follows. Section 2 gives a brief description of the UK's Earth System Model (UKESM1) and the experimental design used in this study. Results can be found in Sect. 3 while conclusions and a discussion can be found in Section 4.

2. Model Description and Experimental Design

The model used in this study is the atmospheric and land components of the UK's Earth System Model, UKESM1 (Sellar et al., 2019). It has a resolution of N96L85, equivalent to a horizontal resolution of approximately 135 km, with 85 hybrid height levels covering an altitude range from the surface up to the model lid at 85 km. The model includes a troposphere-stratosphere chemistry scheme (Archibald et al., 2020) from the United Kingdom Chemistry and Aerosol (UKCA) model (Morgenstern et al., 2009; O'Connor et al., 2014) coupled to a two-moment aerosol scheme called GLOMAP-mode (Mann et al., 2010; Mulcahy et al., 2018, 2020). A full description and evaluation of the gas-phase chemistry and aerosol schemes in UKESM1 can be found in Archibald et al. (2020) and Mulcahy et al. (2020), respectively.

Here, UKESM1 is run in an atmosphere-only configuration, using sea surface temperatures, sea ice conditions, surface water dimethyl sulfide and chlorophyll concentrations, vegetation distribution, leaf area index, and canopy heights representative of the PI (Year 1850) period. These climatologies, including a seasonal cycle, were calculated using 30 years output from the coupled (atmosphere-ocean) PI control experiment of UKESM1 (*piControl*), characterized in Sellar et al. (2019) and run as part of the 6th Coupled Model Intercomparison Project (CMIP6; Eyring et al., 2016).

The experiments conducted here consist of paired simulations: a PI (Year 1850) timeslice simulation and a parallel simulation, in which the global mean CH_4 concentration prescribed as a lower boundary condition in the model is changed from its Year-1850 value (808 ppb) to its PD (Year 2014) value (1,831 ppb) based on CMIP6 recommendations from Meinhausen et al. (2017). CH_4 concentrations aloft are simulated interactively by the model. The initial pair follows the AerChemMIP protocol (Collins et al., 2017) and are called *piClim-control* and *piClim-CH4*, respectively. All other model settings in the experiments are representative of the PI period using CMIP6 recommendations. Briefly here, other GHG concentrations are prescribed according to Meinhausen et al. (2017). Gas-phase and aerosol-phase anthropogenic and biomass burning emissions for the PI period are taken from Hoesly et al. (2018) and van Marle et al. (2017), respectively. Natural volcanic and solar forcings were fixed in all simulations at Year-1850 levels (Arfeuille et al., 2014; Matthes et al., 2017; Thomason et al., 2018) using those specified for CMIP6 (Eyring et al., 2016). Further details are provided in O'Connor et al. (2021).

The apportionment of the total CH_4 ERF between direct and indirect ERFs is calculated in two ways. The first approach is called the "Elimination Method," whereby additional pairs of simulations incrementally disable an interaction or forcing agent from influencing the TOA radiative fluxes, until the last pair only allows CH_4 itself to affect the TOA, thereby giving the direct CH_4 ERF. The difference between successive pairs is then used to

Table 1
List of All the Atmosphere-Only Simulations Carried Out With UKESM1 to Diagnose the Apportionment of the Pre-Industrial (PI; Year 1850) to Present-Day (PD; Year 2014) Effective Radiative Forcing (ERF) From Methane (CH_4) Using the "Elimination Method" and the "Single Forcing Method"

Pair	Experiment	Simulation identifier	CH_4	Other GHGs	Aerosol precursors	Trop. O_3 precursors	Forcing agents or interactions active
Elimination method #1*	*piClim-control**	u-by903	1850	1850	1850	1850	CH_4, WV, O_3, ari, aci
	*piClim-CH4**	u-bz253	2014	1850	1850	1850	
Elimination method #2	*Control*	u-by906	1850	1850	1850	1850	CH_4, WV, O_3, ari
	CH_4 perturbation	u-bz254	2014	1850	1850	1850	
Elimination method #3	*Control*	u-bz144	1850	1850	1850	1850	CH_4, WV, O_3
	CH_4 perturbation	u-bz256	2014	1850	1850	1850	
Elimination method #4	*Control*	u-bz257	1850	1850	1850	1850	CH_4, WV
	CH_4 perturbation	u-bz258	2014	1850	1850	1850	
Elimination method #5 or single forcing method #1	*Control*	u-bz304	1850	1850	1850	1850	CH_4
	CH_4 perturbation	u-bz305	2014	1850	1850	1850	
Single forcing method #2	*Control*	u-bz391	1850	1850	1850	1850	WV
	CH_4 perturbation	u-bz392	2014	1850	1850	1850	
Single forcing method #3	*Control*	u-bz371	1850	1850	1850	1850	O_3
	CH_4 perturbation	u-bz372	2014	1850	1850	1850	
Single forcing method #4	*Control*	u-bz386	1850	1850	1850	1850	ari
	CH_4 perturbation	u-bz387	2014	1850	1850	1850	
Single forcing method #5	*Control*	u-bz389	1850	1850	1850	1850	aci
	CH_4 perturbation	u-bz390	2014	1850	1850	1850	

Note. The table also includes the unique Simulation Identifier for each experiment. All experiment names are in italics following the convention used for experiment names in AerChemMIP (Collins et al., 2017).

*The corresponding data references are O'Connor (2019a, 2019b), respectively. Only Those Simulations Labeled Elimination Method Pair #1 are AerChemMIP Experiments.

infer the proportion of the total CH_4 ERF to that particular indirect effect, forcing agent or interaction assuming linearity.

As mentioned, the final pair above gives the direct CH_4 ERF. Similarly, other paired experiments are conducted, such that the ERF associated with a single composition change or interaction is calculated directly rather than inferring it from differencing two pairs. This methodology is referred to as the "Single Forcing Method" and gives rise to smaller errors than the "Elimination Method." All the experiment pairs carried out for this study using the two methods are listed in Table 1 and were run for 45 years, with the latter 30 years used for analysis.

The ERF itself is calculated from the difference in the TOA radiative fluxes between a perturbation experiment (e.g., *piClim-CH4*) and its control experiment (e.g., *piClim-control*) as follows:

$$\mathrm{ERF} = \Delta F \tag{2}$$

where ΔF includes the IRF as well as other changes to the TOA radiative fluxes due to rapid adjustments. Although strictly by definition, the ERF should exclude land surface temperature adjustments, model experimental protocols and recommendations for quantifying ERFs to date (e.g., Collins et al., 2017; Forster et al., 2016; Pincus et al., 2016) fix sea surface and sea ice conditions only. Hence, the ERFs quantified here include a contribution from temperature adjustments over the land surface. However, this contribution was found to be small in the case of the CH_4 ERF – typically 0.02–0.03 W m^{-2} (Thornhill, Collins, Kramer, et al., 2021) but is much larger for CO_2 forcing (Andrews et al., 2021).

Table 2
Effective Radiative Forcing (ERF) and Its Clear-Sky (CS) and Cloud Radiative Effect (CRE) Components in the Longwave (LW) and Shortwave (SW) Based on Equation 7 and Including an Estimate of the Standard Error, Calculated at the Present Day (PD; Year 2014) Relative to the Pre-Industrial Period (PI; Year 1850) From a PI-to-PD Methane (CH_4) Perturbation in Concentration Using the "Elimination Method" Pairs in Table 1

Forcing agents and/or interactions active	Present day (PD; year 2014) effective radiative forcings (ERFs) relative to the pre-industrial (PI; year 1850) period (W m^{-2})						
	NET ERF	LWcs'	SWcs'	LW ΔCRE'	SW ΔCRE'	NETcs'	NET ΔCRE'
CH_4, WV, O_3, ari, aci	0.97 ± 0.04	0.74 ± 0.02	0.11 ± 0.02	−0.39 ± 0.02	0.50 ± 0.02	0.85 ± 0.03	0.12 ± 0.02
CH_4, WV, O_3, ari	0.69 ± 0.04	0.72 ± 0.03	0.11 ± 0.02	−0.38 ± 0.02	0.24 ± 0.03	0.83 ± 0.03	−0.14 ± 0.03
CH_4, WV, O_3	0.74 ± 0.04	0.77 ± 0.03	0.10 ± 0.02	−0.35 ± 0.02	0.23 ± 0.04	0.87 ± 0.03	−0.12 ± 0.04
CH_4, WV	0.61 ± 0.03	0.58 ± 0.02	0.08 ± 0.01	−0.31 ± 0.02	0.26 ± 0.03	0.66 ± 0.03	−0.05 ± 0.03
CH_4 *only*	0.54 ± 0.04	0.60 ± 0.02	0.07 ± 0.02	−0.26 ± 0.02	0.12 ± 0.04	0.68 ± 0.03	−0.14 ± 0.04

Note. ERFs for individual forcing agents and/or interactions are inferred by differencing the ERF between two successive "Elimination Method" pairs. The CS components include the contribution from aerosol-radiation interactions (ari) while the CRE components are calculated by excluding ari, as recommended by Ghan (2013) – the resulting components are denoted using the prime notation.

The ERF can be decomposed into the clear-sky (CS) component (ERFcs) and the change in the cloud radiative effect (CRE) (ΔCRE) as follows:

$$\mathrm{ERF} = \Delta F\mathrm{cs} + \Delta(F - F\mathrm{cs}) \tag{3}$$

$$= \mathrm{ERFcs} + \Delta\mathrm{CRE} \tag{4}$$

where Fcs is the CS radiative flux. Due to the potential of the CH_4 perturbation to alter atmospheric oxidants and secondary aerosols in UKESM1 leading to "cloud masking" (e.g., Zelinka et al., 2014), ΔCRE is diagnosed from "clean" radiation calls that exclude ari, as recommended in Ghan (2013), with this version of ΔCRE being denoted as ΔCRE′:

$$\mathrm{ERF} = \Delta(F - F\mathrm{clean}) + \Delta F\mathrm{cs,clean} + \Delta(F\mathrm{clean} - F\mathrm{cs,clean}) \tag{5}$$

$$\mathrm{ERF} = \mathrm{Aerosol\,IRF} + \mathrm{ERFcs,clean} + \Delta\mathrm{CRE}) \tag{6}$$

$$\mathrm{ERF} = \mathrm{ERFcs}' + \Delta\mathrm{CRE}) \tag{7}$$

The ERF is, thus, separated into a component due to cloud property changes (ΔCRE′) and the non-cloud forcing (ERFcs′). Here, ERFcs) is the sum of the aerosol IRF and any non-aerosol changes in CS fluxes (due to CH_4, O_3, etc.) and differs slightly from ERFcs in Equation 4, in that it can include the impact of aerosol scattering and absorption in the clear-air above or below clouds. This is the approach adopted by O'Connor et al. (2021) in quantifying a wide range of PD anthropogenic ERFs in UKESM1. However, it is worth noting that ΔCRE′, as defined here, differs from the cloud adjustment in Thornhill, Collins, Kramer, et al. (2021). In that study, the cloud adjustment is estimated from ΔCRE′ but corrects for cloud masking using kernel-derived non-cloud adjustments and the non-aerosol IRF.

For each pair in Table 1, the ERF is calculated as the time-mean global-mean difference in the TOA radiative fluxes, using the latter 30 years of the 45-year long simulations and decomposed into its components following Equation 7 and O'Connor et al. (2021). In addition to the "Elimination Method" and "Single Forcing Method" simulation pairs (Table 1), the TOA IRF from the CH_4-driven changes in aerosols was diagnosed through a double call to the radiation scheme (Ghan et al., 2012) in order to quantify the contribution of the aerosol IRF to ERFcs′ in Equation 7. ERF estimates and their components from the different methods can be found in Tables 2 and 3 and will be discussed in Section 3.

The UKESM1 simulations conducted here (Table 1) were also complemented with offline calculations using the ESM's radiation scheme SOCRATES (Suite of Community Radiation Codes based on Edwards & Slingo, 1996). The offline SOCRATES experimental setup followed the PI aerosol- and cloud-free protocol from the Radiative Forcing Model Intercomparison Project (RFMIP; Pincus et al., 2016), designed to test the accuracy of CS radiative transfer parameterizations on global scales. The setup consists of 100 profiles of PI atmospheric conditions

Table 3
Effective Radiative Forcing (ERF) and Its Clear-Sky (CS) and Cloud Radiative Effect (CRE) Components in the Longwave (LW) and Shortwave (SW) Based on Equation 7 and Including an Estimate of the Standard Error, for Individual Forcing Agents and/or Interactions (Methane (CH_4), Ozone (O_3), Stratospheric Water Vapor (WV), Aerosol-Radiation Interactions (ari), and Aerosol-Cloud Interactions (aci)) Calculated at the Present Day (PD; Year 2014) Relative to the Pre-Industrial Period (PI; Year 1850) From a PI-to-PD Methane (CH_4) Perturbation in Concentration Using the "Single Forcing Method"

Forcing agent and/or interactions active	Present day (PD; Year 2014) effective radiative forcings (ERFs) relative to the pre-industrial (PI; Year 1850) period (Wm^{-2})						
	NET ERF	LWcs'	SWcs'	LW ΔCRE'	SW ΔCRE'	NETcs'	NET ΔCRE'
CH_4 only	0.54 ± 0.04	0.60 ± 0.02	0.07 ± 0.02	−0.26 ± 0.02	0.12 ± 0.04	0.68 ± 0.03	−0.14 ± 0.04
WV only	0.02 ± 0.04	0.03 ± 0.03	−0.01 ± 0.02	−0.02 ± 0.02	0.02 ± 0.04	0.02 ± 0.02	0.00 ± 0.03
O_3 only	0.20 ± 0.04	0.17 ± 0.02	0.07 ± 0.02	−0.10 ± 0.01	0.06 ± 0.04	0.24 ± 0.03	−0.04 ± 0.04
ari only	0.00 ± 0.04	0.03 ± 0.02	0.04 ± 0.02	0.01 ± 0.02	−0.08 ± 0.03	0.07 ± 0.02	−0.07 ± 0.03
aci only	0.30 ± 0.04	0.03 ± 0.03	0.00 ± 0.02	−0.01 ± 0.02	0.28 ± 0.03	0.03 ± 0.02	0.27 ± 0.03

Note. The CS components include the contribution from ari while the CRE components are calculated by excluding ari, as recommended by Ghan (2013) – the resulting components are denoted using the prime notation.

including GHG concentrations (called *PI* here), that when weighted appropriately and averaged, approximate to global annual mean PI radiative fluxes. A parallel perturbation setup consists of an atmosphere, in which all conditions remain at PI levels except for a PI-to-PD perturbation in CH_4 concentration (called *PI-CH4*). Together, *PI* and *PI-CH4* are representative of the UKESM1 simulations *piClim-control* and *piClim-CH4*, respectively, and the difference in radiative fluxes gives the direct CH_4 IRF. A second perturbation setup is representative of a PI atmosphere, but the only perturbation applied is the CH_4-driven O_3 change diagnosed from UKESM1 (called *PI-O3*). Together, *PI* and *PI-O3* mimic the Single Forcing Method #3 pair of UKESM1 simulations (Table 1) and the difference in radiative fluxes yields the indirect O_3 IRF. In a similar way, the indirect WV IRF can be diagnosed by quantifying the difference in radiative fluxes between *PI* and *PI-WV*, where *PI-WV* is representative of a PI atmosphere but with the CH_4-driven change in WV diagnosed from UKESM1 applied.

3. Results

The total PD (Year 2014) CH_4 ERF relative to the PI (Year 1850) period is 0.97 ± 0.04 W m^{-2} (O'Connor et al., 2021, Table 2), where the 0.04 W m^{-2} is the standard error following Forster et al. (2016). Previous studies have found that CH_4 forcing is almost double that of the direct CH_4 forcing (Myhre et al., 2013; Shindell et al., 2005). This is also evident here, with the direct CH_4 ERF estimated to be half (0.54 ± 0.04 W m^{-2}; Table 2) that of the total CH_4 ERF due to indirect effects. These indirect effects result from changes in O_3, stratospheric WV, and potentially aerosols. Tables 2 and 3 provide the indirect ERFs from O_3 and WV; estimates from the two methods agree to within their error bars: 0.13 ± 0.05 W m^{-2} from the Elimination Method and 0.20 ± 0.04 W m^{-2} from the Single-Forcing Method for O_3 and 0.07 ± 0.05 W m^{-2}/0.02 ± 0.04 W m^{-2} for WV.

The ERF estimates also suggest that the total CH_4 ERF from UKESM1 includes a significant indirect contribution from aerosols, particularly aci. As was the case for O_3 and WV, the indirect ERFs from the two methods agree to within their error bars for both aci (0.28 ± 0.06 W m^{-2} from the Elimination Method and 0.30 ± 0.04 W m^{-2} from the Single Forcing Method; Tables 2 and 3) and ari (−0.05 ± 0.06 W m^{-2}/0.00 ± 0.04 W m^{-2}). The results also indicate that the direct and indirect ERFs are additive and that they add up linearly. For example, the total CH_4 ERF (0.97 ± 0.04 W m^{-2}; Table 2) closely matches the sum of the individual direct and indirect ERFs (1.06 ± 0.09 W m^{-2}; Table 3).

Apportionment of the forcing using the Elimination and Single-Forcing pairs in this way may help to explain some of the spread in PD CH_4 ERF estimates from the AerChemMIP multi-model ensemble (Thornhill, Collins, Kramer, et al., 2021) and provide a process-based understanding of the positive cloud adjustment in UKESM1. The direct CH_4 ERF and the indirect ERFs from O_3, WV, and aerosols in UKESM1 and the relevant changes in composition are discussed further in the following sections.

3.1. Composition Changes

Figure 1 shows multi-annual mean PI (*piClim-control*) distributions of O_3, WV, Aitken and accumulation mode aerosol number concentrations, and aerosol optical depth (AOD), as well as changes due to the PI-to-PD increase in CH_4 concentration (*piClim-CH4* minus *piClim-control*). It shows that in the PI atmosphere, O_3 concentrations show a maximum in the tropical stratosphere of greater than 10 ppmv, with minimum concentrations aloft and in the troposphere (Figure 1a). As a tropospheric O_3 precursor, the CH_4 increase gives rise to an increase in tropospheric O_3 concentrations of 10%–20% on a zonal annual mean basis (Figure 1b). Reductions of 0%–10% in stratospheric O_3 concentrations also occur, reflecting the complex interactions between CH_4 and stratospheric O_3 due to both the direct impact of CH_4 on the odd hydrogen loss cycle (Pawson et al., 2014) and the indirect impact of CH_4-induced increases in stratospheric WV (e.g., Stenke and Grewe, 2005). This reduction is lower than the 15% reduction in O_3 following a 2-fold increase from PD CH_4 concentrations in Winterstein et al. (2019) although their simulations had PD chlorine loading. They also showed increases in WV of up to 50% in the middle and higher stratosphere. Here, the CH_4 perturbation represents more than a doubling of the global mean PI concentration and we find maximum increases in WV of over 30% (Figure 1d). The CH_4 perturbation also gives rise to changes in other oxidants (e.g., OH), causing the total CH_4 lifetime to increase from 8.1 years in *piClim-control* to 9.8 years in *piClim-CH4* (O'Connor et al., 2021). In turn, this change in oxidants leads to a change in the global distribution of AOD. In particular, the low background aerosol loading in the PI atmosphere, which has implications for PD anthropogenic aerosol forcing (Carslaw et al., 2013), sees some regional increases and decreases of over 5% in magnitude (Figure 1j). Indeed, Shindell et al. (2009) found an aerosol forcing attributable to a PI-to-PD change in CH_4 although in that study, a change in sulfate burden on a global scale was more evident (−11%). Here, the global mean AOD changes by less than 2%; the regional changes are limited in spatial extent and statistical significance, and have opposing signs.

However, in contrast to the AOD differences, the CH_4-driven changes in the aerosol size distribution are statistically significant. For example, PI Aitken mode number concentrations peak at more than 1,000 cm^{-3} in the tropical mid-troposphere (Figure 1e). The PI-to-PD CH_4 concentration perturbation leads to reductions in Aitken mode number concentrations throughout the troposphere that are statistically significant, with a maximum reduction of up to 50 cm^{-3} (Figure 1f). Likewise, accumulation mode number concentrations peak near the surface in the tropics and the northern hemisphere mid-latitudes in the PI period (Figure 1g), with values of over 100 cm^{-3} and statistical significant reductions of up to 10 cm^{-3} in the lower and mid troposphere result from the CH_4 perturbation (Figure 1h). Given the weak and limited spatial extent of the changes in AOD, these significant reductions in Aitken and accumulation mode number concentrations are commensurate with increases in coarse mode number concentration (not shown). These results support the findings that the indirect contribution to the total PD CH_4 ERF from ari in UKESM1 is small (Tables 2 and 3) and that the CH_4-driven change in the aerosol size distribution has the potential to contribute significantly to the CH_4 ERF through aci (Tables 2 and 3). This is explored further in Section 3.4.

3.2. Direct Methane Effective Radiative Forcing (ERF)

The direct CH_4 ERF at the PD relative to the PI period is 0.54 ± 0.04 W m^{-2} (Tables 2 and 3), consistent with the traditional stratospherically adjusted radiative forcing (SARF) estimate from the updated expression from Etminan et al. (2016) of 0.56 W m^{-2}. As was the case for the total CH_4 ERF (Table 2), the majority of this forcing is in the clear sky (CS) longwave (LW) component (0.60 ± 0.02 W m^{-2}), with the CS shortwave (SW) contribution to the ERF (0.07 ± 0.02 W m^{-2}) being more than offset by the CRE (−0.14 ± 0.04 W m^{-2}). The negative CRE in the direct CH_4 ERF from UKESM1 is consistent with Smith et al. (2018). In that study, only those models that included SW absorption by CH_4 had a negative cloud adjustment; the SW absorption causes tropospheric heating and reductions in upper tropospheric cloud amounts. However, in comparing with the direct CH_4 ERF from the HadGEM2 model (Collins et al., 2011) from Andrews (2014) in Table 4, there is good quantitative agreement between the net CS (0.68 ± 0.03 cf. 0.61 W m^{-2}) and the net CRE (−0.14 ± 0.04 cf. −0.11 W m^{-2}) components. However, there is poor agreement with the individual CS SW (0.07 ± 0.02 cf. −0.13 W m^{-2}) and LW (0.60 ± 0.02 cf. 0.74 W m^{-2}) components, which cannot be reconciled by the different years representing the PI and PD in the two studies. Indeed, UKESM1 shows a positive CS forcing in the SW consistent with Etminan et al. (2016) whereas HadGEM2 has a non-zero CS forcing despite no treatment of solar absorption by CH_4. HadGEM2 also shows a larger CS LW forcing than UKESM1, which could be related to the lack of treatment of

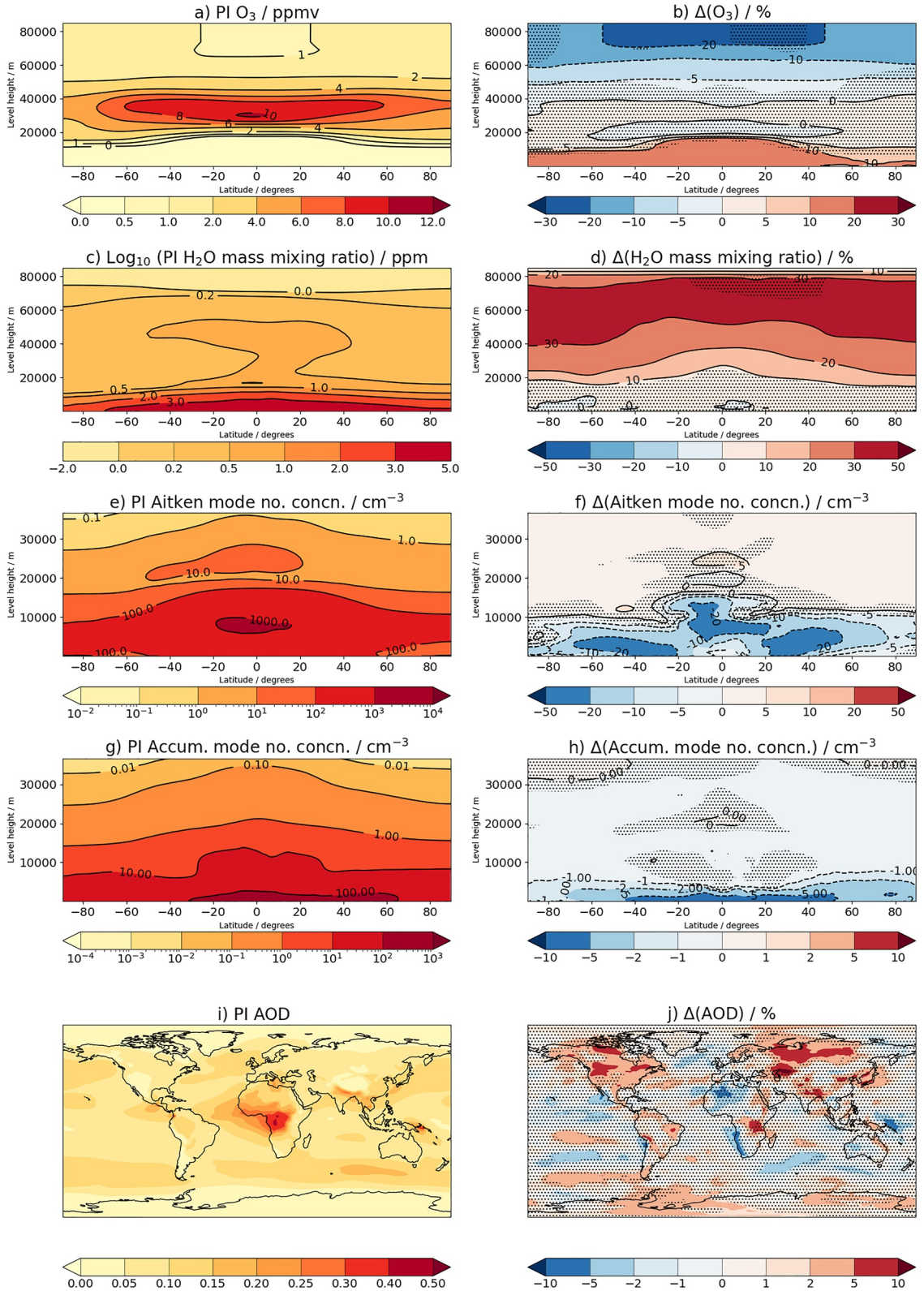

Figure 1.

Table 4
Comparison of the Different Components of the Direct CH_4 ERF at the Present Day (PD) Relative to the Pre-Industrial (PI) Period From HadGEM2 (Andrews, 2014) and UKESM1 (This Study)

			Present day (PD) direct CH_4 effective radiative forcings (ERFs) relative to the pre-industrial (PI) period (W m^{-2})						
Model	PI year	PD year	NET ERF	LWcs'	SWcs'	LW ΔCRE'	SW ΔCRE'	NETcs'	NET ΔCRE'
HadGEM2	1860	2005	0.50	0.74	−0.13	−0.23	0.12	0.61	−0.11
UKESM1	1850	2014	0.54 ± 0.04	0.60 ± 0.02	0.07 ± 0.02	−0.26 ± 0.02	0.12 ± 0.04	0.68 ± 0.03	−0.14 ± 0.04

Note. Different years represent the PD and the PI period in the two studies.

CH_4 in the SW (Collins et al., 2006; Etminan et al., 2016; Li et al., 2010). However, the anomalous negative CS SW component in the HadGEM2 simulations offsets its stronger positive CS LW component, resulting in the two models having comparable net CS components for the direct CH_4 ERF.

To investigate the differences between HadGEM2 and UKESM1 further, we make use of the study by Smith et al. (2018) which found that the direct CH_4 ERF is approximately equal to its IRF, due to the rapid adjustments included in the ERF either being small or summing to zero. As a result, the idealized stand-alone PI test case from the RFMIP protocol (Pincus et al., 2016) can be used here to investigate the differences in the direct CH_4 ERF CS components between HadGEM2 and UKESM1.

As outlined in Section 2, the main test case used from RFMIP is that of a cloud-free aerosol-free PI atmosphere - referred to here as *PI*. A parallel perturbation test case (*PI-CH4*) with the PI-to-PD perturbation applied was set up, with both test cases run using the corresponding spectral data files from HadGEM2 and UKESM1. Figure 2 shows profiles of the differences in the SW, LW and net outgoing radiative fluxes between the two test cases (*PI-CH4* minus *PI*). It shows that with the HadGEM2 spectral data, the SW IRF at TOA under aerosol-free cloud-free conditions is expected to be zero. It also shows that the small positive CS SW ERF from the UKESM1 simulation is consistent with the SW IRF at TOA calculated offline. Looking at the LW fluxes, the difference in the CS LW ERF between HadGEM2 and UKESM1 is mostly explained by the updated spectroscopic data used in UKESM1 relative to HadGEM2 (Walters et al., 2019), although some discrepancy (~0.06 W m^{-2}) still remains. A sensitivity test with offline SOCRATES using 3D CH_4 fields from UKESM1 rather than constant CH_4 concentrations throughout the depth of the atmosphere, at most, accounts for only 0.01 W m^{-2}.

Although the stand-alone tests support the findings from UKESM1 in both the CS SW and LW components of the direct CH_4 ERF, they do not explain the non-zero (or negative) CS SW forcing in HadGEM2. Further investigations into the HadGEM2 simulations show that the negative CS SW ERF was due to changes in dust outflow from North Africa; the 3 CH_4 perturbation experiments showed significant variability in the CS SW ERF that is, −0.04 to −0.28 W m^{-2}, with the −0.13 W m^{-2} reported in Andrews (2014) being the average of the three ensemble members. It is still unclear what mechanism is driving the dust response in HadGEM2 but dust production in that model was found to be highly sensitive to various atmospheric and surface variables (Collins et al., 2011). Nevertheless, the results indicate that the direct CH_4 ERF is better represented in UKESM1 than in HadGEM2 and is more consistent with the Etminan et al. (2016) expression based on line-by-line radiative transfer calculations. UKESM1 is also more consistent with the multi-model mean of the IRF due to a PD-to-PI CH_4 perturbation from present day conditions in Pincus et al. (2020). This improvement in UKESM1 is three-fold: (a) the inclusion of SW absorption by CH_4, (b) the update to the LW spectral data for CH_4, and (c) the absence of an anomalous dust response in the UKESM1 CH_4 perturbation experiments.

3.3. Methane-Driven Ozone and Water Vapor ERFs

As seen from Figure 1, the PI-to-PD perturbation increases tropospheric O_3 and decreases stratospheric O_3, changes which together contribute an indirect O_3 ERF to the total CH_4 ERF. Using the "Elimination Method" and

Figure 1. Multi-annual zonal mean distributions of (a) O_3, (c) water vapor (WV), (e) Aitken mode aerosol number concentration, (g) Accumulation mode aerosol number concentration, and multi-annual global distribution of (i) aerosol optical depth (AOD) in the pre-industrial (PI; Year 1850) period. The relative changes in O_3, WV and AOD due to the increase in CH_4 concentration between the PI and the present day (Year 2014) are shown in (b), (d), and (j), respectively, while the absolute changes in Aitken and Accumulation mode aerosol number concentrations are shown in (f) and (h), respectively. Stippled areas show where the differences are not statistically significant at the 95% confidence interval.

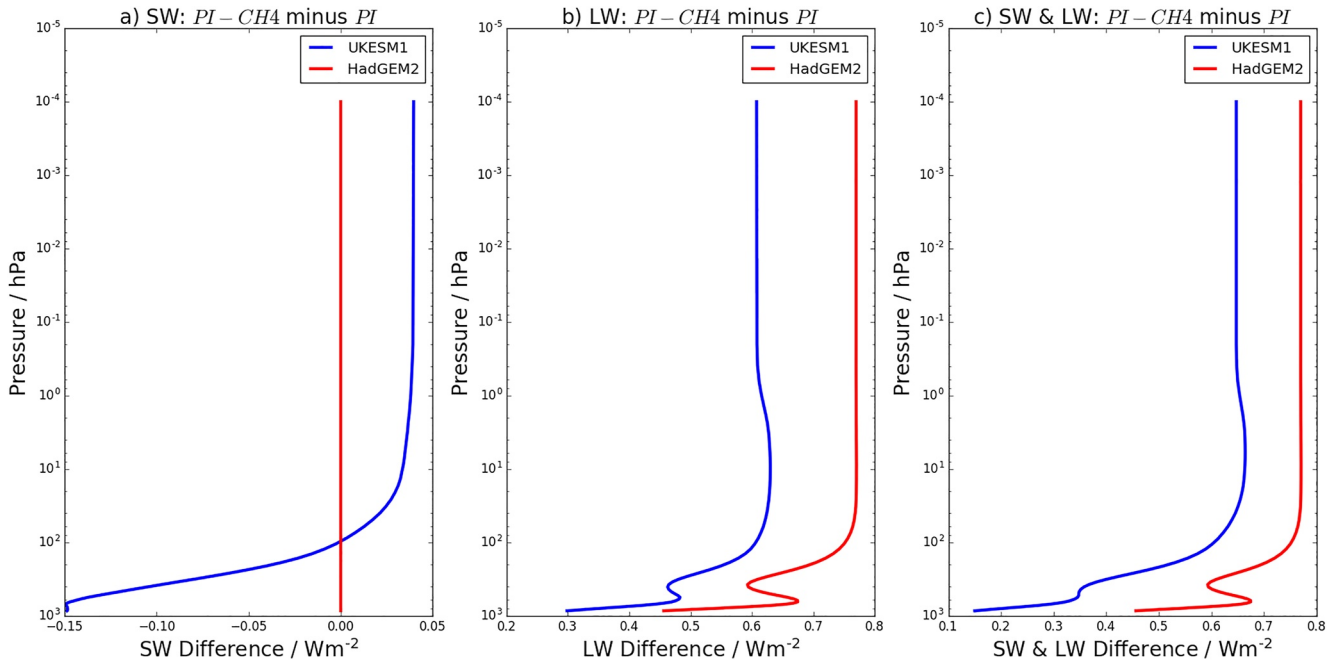

Figure 2. Comparison between two test cases pre-industrial ((*PI*) and *PI-CH4*) using the stand-alone SOCRATES radiation scheme with spectral data from HadGEM2 and UKESM1. Differences in the net outgoing radiative fluxes are shown for the shortwave (SW) in (a), longwave (LW) in (b), and SW&LW combined in (c), using the sign convention that incoming radiative fluxes are positive and outgoing fluxes are negative.

"Single Forcing Method," we calculate an indirect O_3 ERF attributable to the PI-to-PD change in CH_4 concentration of 0.13 ± 0.05 and 0.20 ± 0.04 W m^{-2}, respectively, showing good consistency between the two methods and with the multi-model estimate of 0.14 ± 0.03 W m^{-2} from Thornhill, Collins, Kramer, et al. (2021). This positive forcing is predominantly in the CS (0.18 ± 0.04/0.24 ± 0.03 W m^{-2}; Tables 2 and 3) and in the LW (0.19 ± 0.02/0.17 ± 0.02 W m^{-2}; Tables 2 and 3), reflecting the sensitivity of forcing per unit mass to the vertical distribution of O_3 changes (Lacis et al., 1990) and the dominance of the tropospheric O_3 change to the ERF (Skeie et al., 2020). There is a very weak CRE (−0.07 ± 0.05/−0.04 ± 0.04 W m^{-2}; Tables 2 and 3) but given the standard errors, its contribution to the indirect O_3 ERF and the total CH_4 ERF can be considered negligible. This is consistent with Skeie et al. (2020), who found that the cloud adjustment associated with O_3 forcing is small (~0.02 W m^{-2}), albeit opposite in sign to that found here.

It is also worth noting that WV production from CH_4 oxidation was switched on when isolating the indirect O_3 ERF using the "Elimination Method" (Table 1). This has the potential for the indirect O_3 ERF to include the radiative effect of O_3 changes resulting from CH_4-driven increases in stratospheric WV (e.g., Stenke and Grewe, 2005) in addition to the radiative effect of more direct CH_4-driven changes in tropospheric and stratospheric O_3. On the other hand, for the "Single Forcing Method," the O_3 ERF was quantified with WV production from CH_4 oxidation switched off. Hence, the smaller magnitude of the inferred O_3 ERF compared with that from the Single Forcing method could be due to a difference in O_3 in the model simulations from WV. However, the magnitude of the difference in the O_3 change was less than 2%, with regional differences of opposing sign; the resulting impact on the estimate of the indirect O_3 ERF can be considered negligible given the magnitude of the errors.

The study by O'Connor et al. (2021) found that the SARF from changes in tropospheric O_3 due to the PI-to-PD change in CH_4 concentration is 0.14 W m^{-2}. Taking a whole-atmosphere perspective, we estimate a whole-atmosphere O_3 SARF attributable to the PI-to-PD change in CH_4 concentration of 0.15 W m^{-2} by combining the O_3 IRF calculated offline using SOCRATES (0.11 W m^{-2}) with the stratospheric temperature adjustment (0.04 W m^{-2}) calculated using a temperature radiative kernel (Smith et al., 2018). This suggests that the contribution from the stratospheric O_3 SARF is at most 0.01 W m^{-2}. It confirms that although the O_3 reductions in the upper stratosphere are substantial (0%–20%), the global mean stratospheric changes contribute little to the indirect whole-atmosphere O_3 SARF. This is as a result of O_3 forcing being dominated by changes in the upper troposphere and lower stratosphere (UTLS) (Lacis et al., 1990; Skeie et al., 2020) and the lack of atmospheric mass

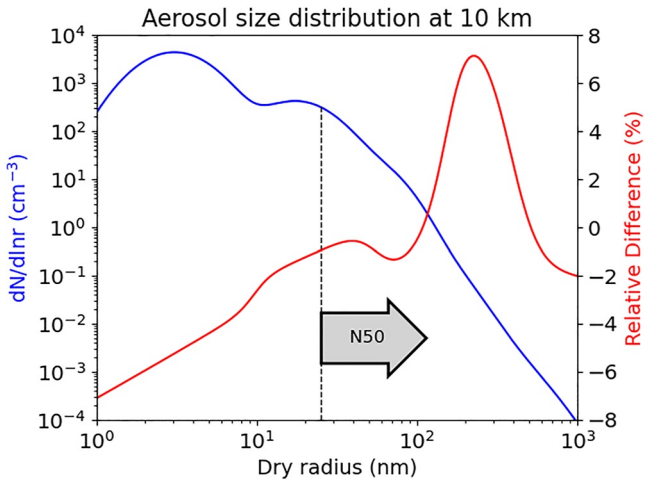

Figure 3. Global annual mean aerosol size distribution at 10 km in altitude in the pre-industrial (PI) atmosphere (blue; left axis) and the relative difference in the size distribution due to the PI-to-present-day perturbation in CH_4 (red; right axis), based on the latter 30 years of the 45-year long simulations. A vertical line marks those particles that are large enough to contribute to N50 in the PI atmosphere.

aloft. However, potential increases in CH_4 beyond the PD may play a more significant role in stratospheric O_3 forcing in the future as concentrations of ozone-depleting substances decrease (e.g., Iglesias-Suarez et al., 2018). In particular, including troposphere-stratosphere chemistry schemes into ESMs (e.g., Morgenstern et al., 2017) provides additional insight into climate change drivers and has greater relevance for policy makers (Shindell et al., 2013).

In addition to O_3, WV is also an effective GHG close to the tropopause (Forster & Shine, 2002; Lacis et al., 1990) and thus WV production from CH_4 oxidation has the potential to exert an indirect forcing. The indirect stratospheric WV ERF estimated here is 0.07 ± 0.05 W m^{-2} and 0.02 ± 0.04 W m^{-2} from the Elimination method and the Single Forcing method, respectively. Previous studies (e.g., Hansen et al., 2005; Myhre et al., 2007) have also found the indirect stratospheric WV SARF to be small; AR5 concluded that it is in the range of 0.02–0.12 W m^{-2} with a central estimate of 0.07 W m^{-2} (Myhre et al., 2013). This is due to the change in WV close to the tropopause being small (Hansen et al., 2005). In this study, the change in the UTLS region is estimated to be less than 10%. Larger changes in WV occur in the upper stratosphere but being optically thin and convectively stable, the changes there are less effective at influencing the radiative balance (Hansen et al., 2005). For comparison purposes, we also quantify the WV SARF in two ways. First, scaling the direct CH_4 SARF of 0.54 W m^{-2} from Etminan et al. (2016) by 15%, as done in the IPCC 4th assessment report (Forster et al., 2007), yields 0.08 W m^{-2}. Second, using the model-diagnosed changes in WV and temperature yield a TOA IRF of 0.05 W m^{-2} and a stratospheric temperature adjustment of 0.04 W m^{-2} from offline SOCRATES and a radiative kernel (Smith et al., 2018), respectively, we estimate a UKESM1-derived SARF of 0.09 W m^{-2}. Both estimates are consistent with the range from previous studies (Hansen et al., 2005; Myhre et al., 2007, 2013). The indirect TOA ERFs quantified here ($0.07 \pm 0.05/0.02 \pm 0.04$ W m^{-2}; Tables 2 and 3) are consistent with each other but in the case of the Single Forcing method, the estimate appears to be marginally weaker than the SARF estimates. This indicates that there may be rapid adjustments other than the stratospheric temperature adjustment and that forcing estimates may be sensitive to the choice of metric (e.g., Smith et al., 2018). Nevertheless, the stratospheric WV forcing here is weakly positive and the choice of forcing metric does not have a major impact on the understanding of the role of CH_4-driven changes in WV in the PD forcing of climate.

3.4. Methane-Driven Aerosol ERF and Cloud Radiative Effect

A significant finding of this study is that increases in CH_4 concentration lead to changes in aerosol properties resulting in a positive contribution to the total CH_4 ERF. This aerosol-mediated term is estimated to be 0.28 ± 0.06 or 0.30 ± 0.06 W m^{-2}, depending on whether the "Elimination Method" or "Single Forcing Method" is used (Tables 2 and 3). This forcing is almost entirely from aci and their influence on the SW radiative effects of clouds. The aci component is estimated to be $0.28 \pm 0.06/0.30 \pm 0.04$ W m^{-2} (Tables 2 and 3) and the ari component is either weakly negative or neutral at $-0.05 \pm 0.06/0.00 \pm 0.04$ W m^{-2} (Tables 2 and 3). A double call to the radiation scheme following Ghan et al. (2012) confirms that the magnitude of the CH_4-driven aerosol IRF is less than 0.01 W m^{-2}, consistent with the near-zero ari term derived from the Elimination and Single-Forcing methods and the AerChemMIP models (Thornhill, Collins, Kramer, et al., 2021). This is also consistent with the global mean AOD change only being of the order of 2% (Figure 1). The explanation for the relatively substantial aci component lies in more subtle changes to aerosol size distributions and number concentrations. These appear to have been triggered by changes in oxidation rates affecting secondary aerosol formation and the nucleation of new particles. These following sub-sections explore these processes in further detail.

3.4.1. Aerosol-Cloud Microphysical Changes

As shown in Figure 1, the PI-to-PD increase in CH_4 leads to statistically significant reductions in aerosol number concentrations, particularly across the Aitken mode, but also in the accumulation mode. This is also clear from examining the aerosol size distribution (Figure 3), where particle concentrations reduce most in relative terms across the size range up to 200 nm in diameter (up to 100 nm radius), encompassing the Aitken mode and much

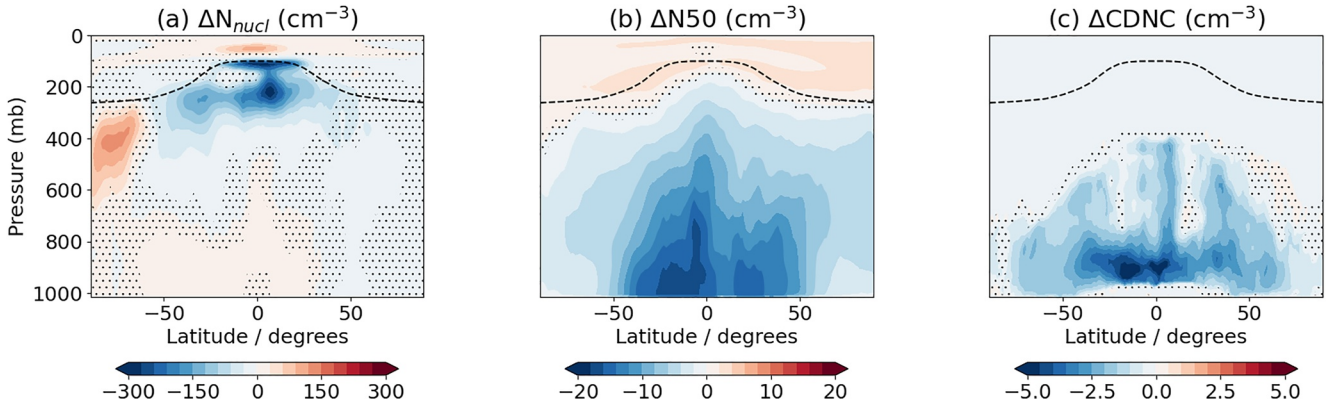

Figure 4. Multi-annual zonal mean changes in aerosol number concentrations, driven by the pre-industrial-to-present-day change in CH_4 concentration in the *piClim-CH4* simulation. Results include changes to (a) nucleation-mode particles, (b) number of particles greater than 50 nm in diameter, and (c) number of particles activated into cloud condensation nuclei. Stippled areas show where the differences are not statistically significant at the 95% confidence interval.

of the accumulation-mode peak. Crucially, the number of particles greater than 50 nm in diameter (N50) has reduced and this is likely to affect the availability of cloud condensation nuclei (CCN). The reduction of particle number concentrations appears to be driven by a reduction in the nucleation of new particles in the upper troposphere (Figure 4a). This is a region of the atmosphere where nucleation is typically most intense in the model so the reduction affects aerosol numbers globally. Indeed, there is a drop in zonal mean N50 across all latitudes and through the depth of the troposphere (Figure 4b). This follows through to a reduction in cloud droplet number concentration (CDNC) across all latitudes and heights in the multi-annual zonal means (Figure 4c) where liquid clouds are present in the model. The changes in N50 vary regionally as do the impacts on CDNC (Figures 5a and 5b). The strongest reductions in CDNC at 1 km occur over the oceans, especially in tropical and sub-tropical latitude zones where stratocumulus typically reside. These are statistically significant across most ocean regions and, as expected, lead to significant increases in cloud droplet effective radius (Reff) at 1 km, averaging around 0.1 − 0.2 μm over much of the oceans (Figure 5c). The results strongly indicate that the so-called Twomey effect (Twomey, 1977) is weakened in the *piClim-CH4* simulation relative to *piClim-control*, resulting in less reflective clouds and the positive indirect ERF from aci of 0.28 ± 0.06/0.30 ± 0.04 W m^{-2} (Tables 2 and 3). Although defined differently, the estimated aci response here is consistent with the UKESM1 cloud adjustment of

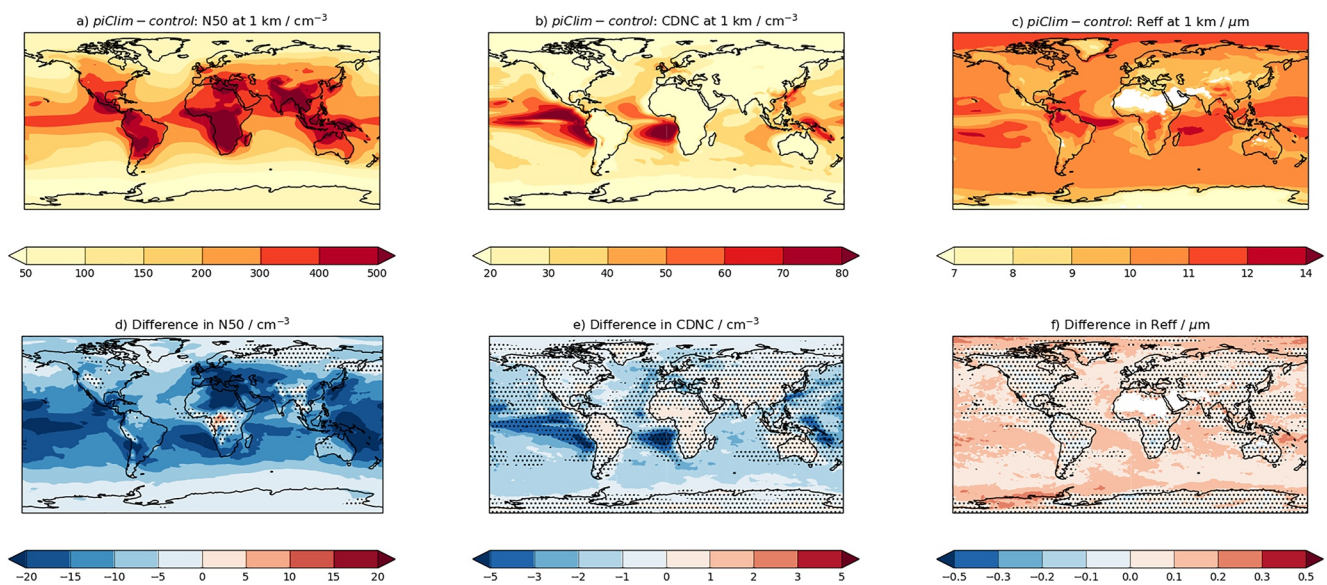

Figure 5. Global distributions of multi-annual mean (a) N50, (b) cloud droplet number concentration (CDNC) and (c) cloud droplet effective radius (Reff) at 1 km height and differences as a result of the pre-industrial-to-present-day perturbation in CH_4 in (d), (e), and (f). Units are in cm^{-3} for N50 and CDNC and in μm for Reff.

0.24 W m^{-2} from the radiative kernel difference method used in Thornhill, Collins, Kramer, et al. (2021) – this is due to the corrections for cloud masking in Thornhill, Collins, Kramer, et al. (2021) canceling out or being equal to zero in the approaches (Elimination Method or Single Forcing Method) used here.

3.4.2. Aerosol-Chemical Feedback Mechanisms

To understand why such changes in aerosol microphysics have occurred requires a more detailed investigation of changes in oxidation rates and the life cycle of aerosol-chemical processes. Table 5 shows a full gas-phase and aerosol budget for sulfur species and organic matter (OM) from the *piClim-control* and *piClim-CH4* simulations and Figure 6 shows a schematic of the main processes involved in the secondary formation of sulfate (SO_4) aerosol in UKESM1 (Sellar et al., 2019). Dimethyl sulfide (DMS) is oxidized in the gas phase to form sulfur dioxide (SO_2). In the PI atmosphere, DMS is oxidized by the hydroxyl (OH) radical (14.38 ± 0.09 Tg (S) yr^{-1}), nitrate (2.03 ± 0.03 Tg (S) yr^{-1}) and oxygen atoms (0.18 ± 0.01 Tg (S) yr^{-1}). Together with carbonyl sulfide (COS) photolysis and oxidation, they account for 16.72 ± 0.10 Tg (S) yr^{-1} of the PI global SO_2 source. The remaining SO_2 source is primary, amounting to 14.82 Tg (S) yr^{-1}. SO_2 is then oxidized by OH and O_3 in the gas phase and by hydrogen peroxide (H_2O_2) and O_3 in the aqueous phase (Table 5), with the 3 principal pathways shown in Figure 7. Oxidation by OH accounts for 40.7% of PI SO_2 oxidation to produce sulfuric acid (H_2SO_4). New particle formation arises from the binary homogeneous nucleation of H_2SO_4 and water in the free troposphere (Vehkamäki et al., 2002), leading to an increase in nucleation mode number concentration and SO_4 aerosol mass (Figure 6) and accounting for 0.8% of PI secondary SO_4 aerosol production. Gas-phase H_2SO_4 also condenses onto pre-existing aerosol, increasing SO_4 mass without changing aerosol number concentration and contributes 46.7% to the secondary SO_4 aerosol production. SO_2 is also oxidized via dissolution into cloud droplets followed by reaction with H_2O_2 or O_3. Fluxes from these aqueous-phase reactions update the SO_4 mass in both the accumulation and coarse mode aerosol with no change in aerosol number concentration, and account for 43.3% and 9.1% of secondary SO_4 production, respectively. The resulting PI SO_4 burden is 0.456 ± 0.005 Tg (S). Wet scavenging accounts for up to 85% of SO_4 aerosol removal, leading to a lifetime of 9.17 ± 0.12 days.

Table 5 indicates that in the PI atmosphere, primary emissions of OM from land and marine sources contribute 49.25 ± 0.01 Tg (OM) yr^{-1}, with the latter coupled to the ocean biogeochemistry scheme (Mulcahy et al., 2020; Sellar et al., 2019). Secondary formation of OM is via oxidation of monoterpenes and the gas-phase product condenses onto pre-existing aerosol (Kelly et al., 2018; Mulcahy et al., 2020) that is, increasing OM aerosol mass but with no change in aerosol number concentration. In the PI atmosphere, secondary formation of OM aerosol accounts for 43.7% of the global OM source. Close to 80% of OM is removed by wet scavenging, with the remainder by dry deposition, leading to a PI aerosol burden of 1.28 ± 0.02 Tg (OM) and a lifetime of 5.29 ± 0.05 days. A full description of the GLOMAP-mode aerosol scheme and its performance in UKESM1 for the recent past can be found in Mulcahy et al. (2020).

In *piClim-CH4*, the PI-to-PD increase in CH_4 concentration does not change the total DMS source or DMS oxidation flux relative to the PI atmosphere (Table 5). However, CH_4-driven changes in oxidants change the relative contributions of the different DMS oxidation pathways. For example, oxidation by OH reduces by 4% while oxidation by NO_3 increases by 22%. These changes are most evident in the DMS burden over the Southern Ocean, where reductions in oxidation by OH change the regional distribution of secondary sources of SO_2 (not shown). On a global annual mean basis, the DMS burden and lifetime both increase (Table 5).

The PI-to-PD increase in CH_4 also alters the relative contribution of the different SO_2 oxidation pathways (Figure 7). Oxidation of SO_2 by OH reduces from 8.01 ± 0.07 Tg (S) yr^{-1} to 6.83 ± 0.06 Tg (S) yr^{-1} - a decrease of 14.7%. Oxidation by H_2O_2 increases by 12.4% and accounts for over 50% of SO_2 oxidation. There is little change in the aqueous-phase oxidation by O_3 (−0.5%) or in the total amount of SO_2 being oxidized, as was the case for DMS. The change in oxidation by OH is consistent with the CH_4 lifetime increasing by 21% in *piClim-CH4* relative to *piClim-control* (O'Connor et al., 2021). Given that the gas-phase oxidation of SO_2 by OH is the only pathway that gives rise to new particle formation in UKESM1, a change in the relative contributions of the different SO_2 oxidation pathways *alone* may lead to a change in aerosol size distribution and hence, cloud activation (Abdul-Razzak & Ghan, 2000). A similar mechanism, albeit due to sensitivity of the aqueous-phase oxidation of SO_2 by O_3 to changes in cloud water pH, was found to affect aerosol formation rates, cloud activation, and aerosol forcing by Turnock et al. (2019) although the pH is fixed in the configuration used here (Mulcahy et al., 2020).

Table 5
Aerosol and Gas-Phase Budget Terms for Dimethyl Sulfide (DMS), Sulfur Dioxide (SO_2), Sulfate (SO_4) Aerosol, and Organic Matter (OM) in UKESM1, Based on the Latter 30 Years of the piClim-control and piClim-CH4 Simulations

		Production (Tg (S) yr^{-1} or Tg (OM) yr^{-1})		Loss (Tg (S) yr^{-1} or Tg (OM) yr^{-1})			Burden (Tg (S) or Tg (OM))	Lifetime (days)
Species	Simulation	Primary	Secondary	Dry deposition	Wet deposition	Oxidation		
DMS	*piClim-control*	16.47 ± 0.09	N/A	N/A	N/A	OH: 14.38 ± 0.09 NO_3: 2.03 ± 0.03 O^3P: 0.18 ± 0.01 Sum: 16.59 ± 0.10	0.09 ± 0.001	2.06 ± 0.03
	piClim-CH4	16.44 ± 0.12	N/A	N/A	N/A	OH: 13.79 ± 0.09 NO_3 2.48 ± 0.03 O^3P: 0.24 ± 0.01 Sum: 16.51 ± 0.11	0.11 ± 0.002	2.38 ± 0.03
SO_2	*piClim-control*	14.82 ± 0.00	DMS + OH: 14.38 ± 0.09 DMS + NO_3: 2.03 ± 0.03 DMS + O^3P: 0.18 ± 0.01 COS Photolysis: 0.02 ± 0.001 COS + O^3P: 0.01 ± 0.001 COS + OH: 0.11 ± 0.001 Sum: 16.72 ± 0.10	5.39 ± 0.04	7.09 ± 0.06	OH (g): 8.01 ± 0.07 O_3 (g): <0.001 H_2O_2 (aq): 9.63 ± 0.05 O_3 (aq): 2.03 ± 0.04 Sum: 19.68 ± 0.08	0.24 ± 0.002	2.74 ± 0.02
	piClim-CH4	14.82 ± 0.00	DMS + OH: 13.79 ± 0.09 DMS + NO_3: 2.48 ± 0.03 DMS + O^3P: 0.24 ± 0.01 COS Photolysis: 0.02 ± 0.001 COS + O^3P: 0.01 ± 0.001 COS + OH: 0.09 ± 0.001 Sum: 16.63 ± 0.11	5.30 ± 0.05	7.09 ± 0.07	OH (g): 6.83 ± 0.06 O_3 (g): <0.001 H_2O_2 (aq): 10.82 ± 0.07 O_3 (aq): 2.02 ± 0.04 Sum: 19.67 ± 0.09	0.25 ± 0.002	2.84 ± 0.02
SO_4	*piClim-control*	0.38 ± 0.00	Nucleation via OH: 0.137 ± 0.003 Condensation via OH: 7.78 ± 0.07 In-cloud via H_2O_2: 7.20 ± 0.04 In-cloud via O_3: 1.52 ± 0.03 Sum: 16.64 ± 0.09	2.60 ± 0.03	14.40 ± 0.05	N/A	0.456 ± 0.005	9.17 ± 0.12
	piClim-CH4	0.38 ± 0.00	Nucleation via OH: 0.126 ± 0.003 Condensation via OH: 6.61 ± 0.06 In-cloud via H_2O_2: 8.08 ± 0.06 In-cloud via O_3: 1.52 ± 0.03 Sum: 16.34 ± 0.09	2.52 ± 0.03	14.24 ± 0.06	N/A	0.446 ± 0.005	8.97 ± 0.12
OM	*piClim-control*	49.25 ± 0.01	Condensation via OH: 10.98 ± 0.17 Condensation via NO_3: 2.92 ± 0.03 Condensation via O_3: 24.34 ± 0.21 Sum: 38.24 ± 0.37	17.79 ± 0.14	69.35 ± 0.32	N/A	1.28 ± 0.02	5.29 ± 0.05
	piClim-CH4	49.25 ± 0.01	Condensation via OH: 10.45 ± 0.16 Condensation via NO_3: 2.98 ± 0.03 Condensation via O_3: 24.92 ± 0.17 Sum: 38.35 ± 0.30	17.78 ± 0.12	69.46 ± 0.24	N/A	1.28 ± 0.02	5.30 ± 0.05

Note. Units of production and loss are in Tg (S) yr^{-1} for the sulfur species and in units of Tg (OM) yr^{-1} for OM, where the ratio of carbon to OM is 1.0:1.4. Units of burden are in Tg (S) or Tg (OM) and the lifetime is in days. Of the aqueous-phase SO_2 oxidation fluxes, 25% of the SO_2 is assumed to re-evaporate from the aqueous phase into the atmosphere and does not form SO_4 aerosol. The corresponding data references for *piClim-control* and *piClim-CH4* are O'Connor (2019a, 2019b), respectively. As was the case in Table 1, the experiment names are in italics following the convention used for experiment names in AerChemMIP (Collins et al., 2017).

Due to oxidant changes, the CH_4 increase in *piClim-CH4* leads to less new particle formation; nucleation rates of H_2SO_4 decrease from 0.137 ± 0.003 to 0.126 ± 0.003 Tg (S) yr^{-1}, amounting to a decrease of 8.0%. This helps to explain why the concentration of nucleation-mode particles has reduced (Figure 4a). Condensation of gas-phase H_2SO_4 also decreases, with the smallest and largest reductions evident in condensation rates onto the

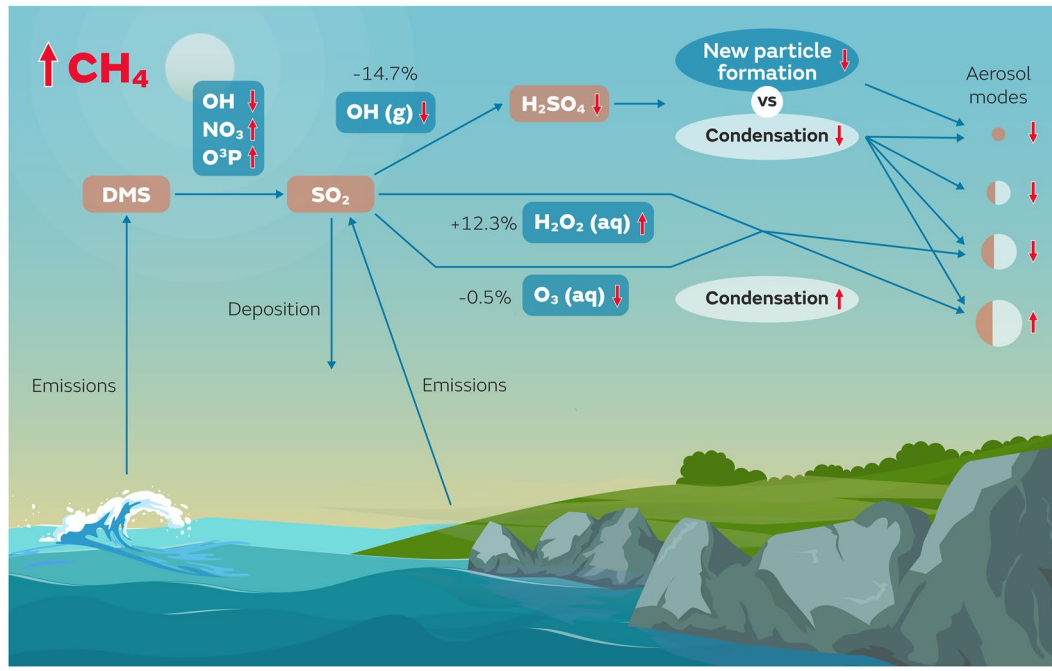

Figure 6. Schematic showing the mechanism for aerosol forcing attributable to methane at the present-day (PD; Year 2014) relative to the pre-industrial (PI; Year 1850). The relative contributions of the different oxidation pathways of sulfur dioxide (SO_2) lead to a change in the aerosol size distribution. Sulfur species include dimethyl sulfide and sulfuric acid (H_2SO_4). Oxidants include hydroxyl (OH), nitrate (NO_3), atomic oxygen (O^3P), hydrogen peroxide (H_2O_2) and ozone (O_3). The numbers in parentheses indicate the percentage of the total SO_2 oxidation that is oxidized through a particular pathway and the percentage below is the relative change in SO_2 oxidation as a result of the increase in methane (CH_4) concentration from PI to PD levels.

nucleation and coarse modes of 8.3% and 21.1%, respectively. On the other hand, condensation rates onto accumulation and coarse mode aerosol following aqueous-phase oxidation of SO_2 via H_2O_2 increase from 7.20 ± 0.04 to 8.08 ± 0.06 Tg (S) yr^{-1}. The net effect of these changes is that there is less SO_4 mass in the nucleation (−1.8%) and accumulation (−3.8%) modes, with a very marginal increase in the Aitken mode (less than 1%) and a near-zero change in the coarse mode. Together, these combine to give a SO_4 burden in *piClim-CH4* of 0.446 ± 0.005 Tg (S), which is only 2% lower than in the PI atmosphere.

In the case of OM, CH_4 changes the relative contributions of the different monoterpene oxidation pathways although the total secondary production of OM is unchanged. Oxidation by OH decreases by 4.8%, while oxidation by NO_3 and O_3 increase by 2.1% and 2.4%, respectively. As a result, the monoterpene burden reduces by 6% in the global annual mean. Secondary OM production, via condensation onto pre-existing aerosol of the condensable vapor product from monoterpene oxidation, remains unchanged (Table 5). However, condensation onto the nucleation and Aitken soluble modes decreases by 4.6% and 1.5%, respectively, while that onto the Aitken insoluble, accumulation and coarse modes increases marginally. This is suggestive that changes in gas-to-particle partitioning of OM onto pre-existing aerosol also have the potential to modulate the aerosol size distribution further. Although the total OM burden is unchanged, there is less OM mass in all modes, except for the Aitken insoluble mode. Less mass in the smaller modes also reduces the condensational growth of particles to sizes that can contribute to CCN, thereby directly leading to a shift in the aerosol size distribution (Figure 3) toward one with fewer particles large enough to act as CCN (Figure 4) and a weakening of the Twomey effect (Section 3.4.1).

3.5. Thermodynamic Feedbacks on Cloud

The analyses presented in Tables 2 and 3 show that the CRE played a significant role in the CH_4 ERF. In total, the CRE accounts for 0.12 W m^{-2} of the total CH_4 ERF (with all interactions included) but the individual SW and LW components are much larger (0.50 W m^{-2} for SW and −0.38 W m^{-2} for LW). Whilst the aci were a strong

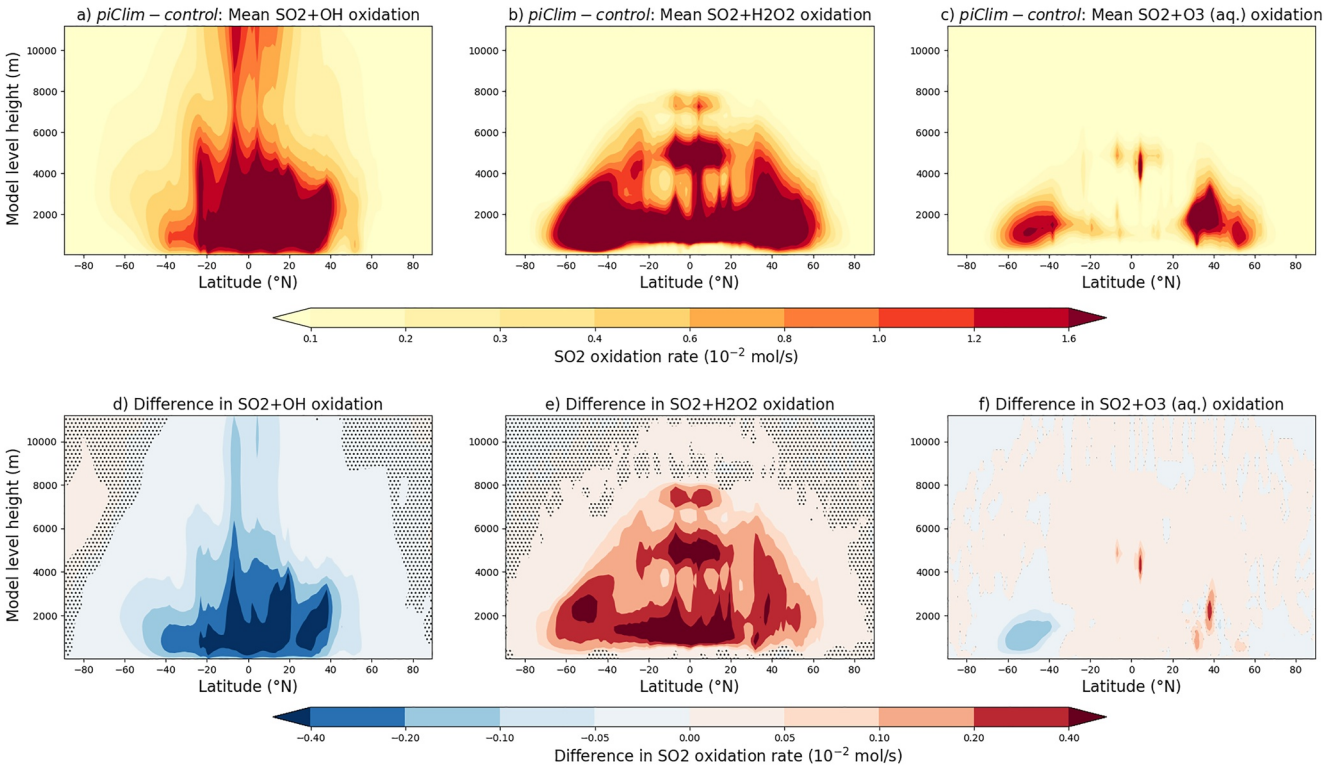

Figure 7. Multi-annual zonal mean distributions of sulfur dioxide (SO_2) oxidation fluxes via (a) hydroxyl (OH), (b) hydrogen peroxide (H_2O_2), and (c) ozone (O_3) in *piClim-control*. The difference in the oxidation rates as a result of the PI-to-PD methane increase is shown in (d), (e), and (f). Units are in 10^{-2} mol (S) per second.

contributor to the SW CRE (amounting to 0.28–0.30 W m^{-2}) and wholly responsible for the cloud adjustment as defined in Thornhill, Collins, Kramer, et al. (2021), some 0.23 W m^{-2} of the SW CRE occurs with aci disabled. The negative LW CRE component is driven almost exclusively by the non-aerosol interactions; the perturbations in CH_4, WV and O_3 together build toward the negative LW CRE of −0.35 W m^{-2} in the absence of the aci. It is therefore clear that much of the change in the CRE are related to thermodynamic feedbacks, such as changes in temperature and atmospheric circulation, rather than microphysical interactions.

To investigate such thermodynamic feedbacks, we analyze the pair of simulations with PI or PD CH_4 where interactive aci were eliminated (as listed in the second row of Table 2). There are increases in temperature in the troposphere (Figure 8a), especially in the upper troposphere and the warming peaks at around 0.5 K across the tropical tropopause. Some cooling occurs at higher levels in the stratosphere. Along with the warming patterns are statistically significant reductions in cloud fractions (Figure 8b). For instance, in the deep tropics, cloud cover has reduced at mid and upper levels of the troposphere, which is indicative of suppressed convection associated with the warming and stabilization of the troposphere. There are also statistically significant reductions in cloud cover in the mid-latitudes around 45°S and 40°N that extend through the range of the troposphere. At high latitudes, there appears to be strong changes in cloud of both positive and negative sign, but these are not statistically significant. Overall, the global-mean cloud fraction reduces by 0.25% and there were decreases of 1.0% and 0.9% in global-mean liquid water path and ice water path, respectively. The decreased cloud explains the negative LW CRE (increased outgoing LW), and positive SW CRE (less reflection). In addition, global-mean precipitation decreases by 0.013 mm/day (0.4%), indicating that there was a slight slowing down of the hydrological cycle. This is consistent with the suppression of convection, which is expected for forcing agents that increase absorption of radiation in the troposphere. The CH_4 contributes SW and LW absorption (Figure 2) and increased tropospheric O_3 contributes to the absorption of SW in the troposphere. These decreases in precipitation, cloud and CRE can be regarded as so-called "rapid responses" (e.g., Smith et al., 2018), since the sea surface temperatures in these simulations were fixed. Slow feedbacks from longer-term climate warming could be different or even have the opposite tendency to the fast feedbacks.

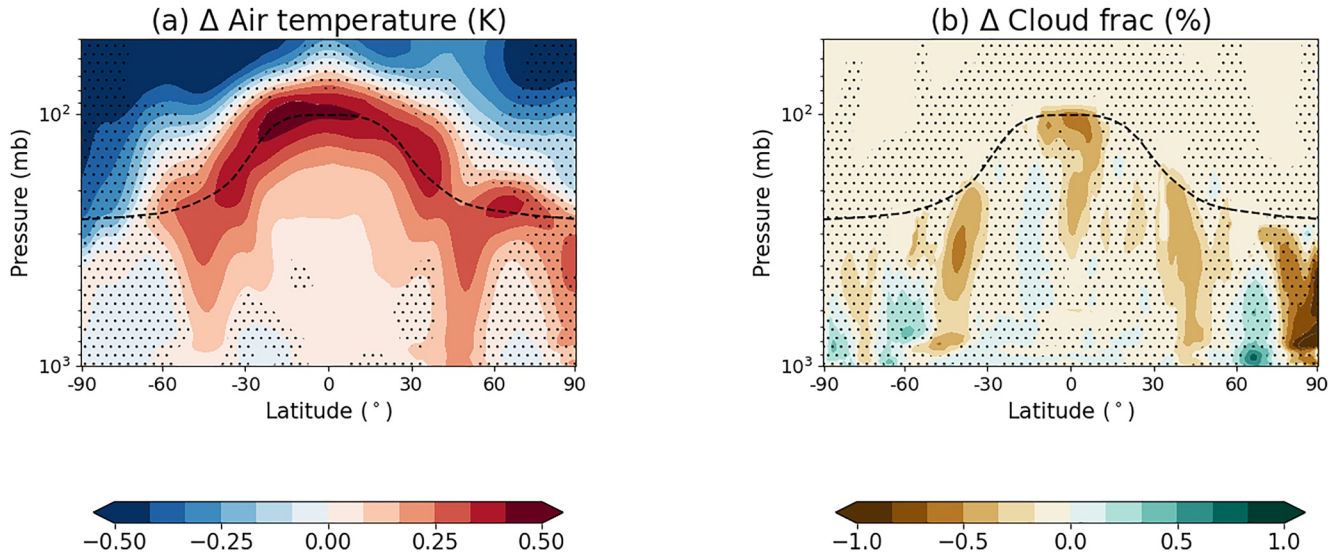

Figure 8. Multi-annual mean zonal mean changes in (a) temperature, (b) cloud fraction from the large-scale stratiform cloud scheme based on the difference between *piClim-CH4* and *piClim-control*, where aerosol-cloud interactions were suppressed.

3.6. Emission-Based Estimates of Forcing

The direct and indirect CH_4 ERFs quantified here are based on the observed change in global mean concentration between 1850 and 2014 (Meinhausen et al., 2017) and are referred to as concentration-based or abundance-based ERFs. The abundance-based approach used here is similar to that taken for previous estimates of the direct and total CH_4 forcing (Andrews, 2014; Etminan et al., 2016; O'Connor et al., 2021; Smith et al., 2018; Thornhill, Collins, Kramer, et al., 2021). However, the chemical coupling between CH_4 and its own sink, via OH, means that an increase in CH_4 emissions decreases OH, increases the CH_4 lifetime, and increases the resulting atmospheric concentration (Prather et al., 2001). The CH_4 lifetime and atmospheric abundance also depend on emissions of other tropospheric O_3 precursors, with the PI-to-PD increase in volatile organic compound (VOC) and carbon monoxide (CO) emissions contributing to an increase in CH_4 lifetime whereas the increase in nitrogen oxides (NOx) emissions causes a decrease (Stevenson et al., 2020). Together, it means that the observed CH_4 concentration change is lower than would arise from the PI-to-PD change in CH_4 emissions *alone*. As a result, an emissions-based forcing estimate, based solely on the PI-to-PD increase in CH_4 emissions, could be larger than an abundance-based estimate by as much as 25% (Shindell et al., 2005).

Outside of CMIP6, ESMs including UKESM1 are starting to include more interactive CH_4 cycles, with CH_4 emissions-driven rather than concentration-driven (Folberth et al., 2022; Kleinen et al., 2020; Ocko et al., 2018). Forcing estimates from an emissions-based perspective, in the case of CH_4, provide a more direct attribution of the forcing to changing emissions and have greater relevance for policy makers (Shindell et al., 2013). Therefore, understanding and quantifying the potential differences in forcing between the current generation of CMIP6 models with CH_4 concentration-driven and those models driven by CH_4 emissions is important. Here, we attempt to convert the UKESM1 direct and indirect abundance-based CH_4 ERFs to emissions-based estimates.

To do this for the direct CH_4 radiative forcing and ERF, we make use of additional experiments from the AerChemMIP protocol (Collins et al., 2017): *piClim-NOx* and *piClim-VOC*, in which PI-to-PD perturbations to the anthropogenic emissions of (a) NOx and (b) VOCs and CO were applied, respectively. The model-diagnosed change in total CH_4 lifetime in relation to *piClim-control* is used to calculate the equilibrium CH_4 concentrations from the *piClim-CH4*, *piClim-NOx* and *piClim-VOC* experiments following O'Connor et al. (2021). From the difference between the prescribed and equilibrium CH_4 concentrations and the UKESM1 direct CH_4 ERF, a PD emissions-based direct radiative forcing by CH_4 is estimated to be 0.67 W m^{-2}. This comprises the direct CH_4 concentration-based radiative forcing of 0.56 W m^{-2} from Etminan et al. (2016) and additional individual contributions from CH_4, NOx, and VOCs/CO (via their influence on CH_4 lifetime) of 0.22, −0.19, and 0.08 W m^{-2}, respectively (Table 6). The estimate of 0.67 W m^{-2} is almost 20% larger than the concentration-based estimate of 0.56 W m^{-2}, and is consistent with the findings of Shindell et al. (2005). Using the direct CH_4 ERF from

Table 6
Table Indicating Prescribed Global Mean CH_4 Concentrations, Total CH_4 Lifetime, Equilibrium CH_4 Concentrations and the Additional RF Contributions From the piClim-NOx, piClim-VOC, and piClim-CH4 Simulations to the Emissions-Based Estimate of the Direct CH_4 RF at the PD (Year 2014) Relative to PI (Year 1850)

Experiment	Prescribed CH_4 concn./ppb	Total CH_4 lifetime/ years	Equilibrium CH_4 concn./ ppb	ΔCH_4/ ppb	Direct ΔCH_4 RF/W m^{-2}
piClim-control	808	8.1	N/A	N/A	N/A
piClim-NOx	808	6.1	563	−245	−0.19
piClim-VOC	808	9.0	928	120	0.08
piClim-CH4	1831	9.8	2364	533	0.22

UKESM1 of 0.54 W m^{-2} (Table 2) and applying the same scaling, the direct emissions-based CH_4 ERF from UKESM1 is 0.65 ± 0.05 W m^{-2}.

In relation to the indirect O_3 forcing from CH_4, the study by O'Connor et al. (2021) found that the tropospheric O_3 SARF for the year 2014 due to changes in CH_4 since the PI period from concentration-based and emissions-based perspectives is 0.14 and 0.21 W m^{-2}, respectively. The emissions-based estimate is comparable to that from Shindell et al. (2005) for the year 1998 (0.20 W m^{-2}) relative to 1750 despite the CH_4 concentration change in that study being larger than that applied here (1,209 cf. 1,023 ppb). However, they noted from their simulations that the O_3 response to a positive CH_4 perturbation at the PI is larger than a negative perturbation applied at the PD by 20%. Therefore, scaling our emissions-based estimate by the ratio of the concentration changes between the two studies gives a revised UKESM1 estimate of 0.25 W m^{-2} for the 1750–1998 period, which is indeed approximately 20% larger than the estimate from their PD simulations. Taking the UKESM1 indirect abundance-based ERFs from O_3 of 0.13 ± 0.05 and 0.20 ± 0.04 W m^{-2} from the Elimination (Table 2) and Single-Forcing (Table 3) methods, respectively, emission-based ERFs are likely to be 0.19 ± 0.07 and 0.30 ± 0.06 W m^{-2}, respectively. These ERF values are reasonably consistent with the SARF of 0.21 W m^{-2} from O'Connor et al. (2021) and reflect that rapid adjustments in the O_3 ERF are small in magnitude and nearly sum to zero (Skeie et al., 2020).

In the case of stratospheric WV, adopting the approach of scaling the direct emissions-based CH_4 ERF of 0.65 W m^{-2} by 15% yields an indirect emissions-based ERF from WV of 0.10 ± 0.01 W m^{-2}. However, this seems rather high relative to the abundance-based ERF from the Single-Forcing Method of 0.02 ± 0.04 W m^{-2} (Section 3.3). Therefore, as an alternative, we apply the ratio of the direct emissions-based to the abundance-based CH_4 ERFs to the indirect abundance-based WV ERF, leading to an estimate of 0.02 ± 0.05 W m^{-2}. Finally, although aci are non-linear, a similar approach leads to a potential emissions-based indirect ERF from aci of 0.35 ± 0.07 and 0.36 ± 0.05 W m^{-2} from the Elimination and the Single-Forcing methods, respectively. Taking the emission-based ERFs from the Single-Forcing method alone, we calculate a total PD (Year 2014) emissions-based CH_4 ERF of 1.33 ± 0.11 W m^{-2} relative to the PI (Year 1850) period. This is higher than the total abundance-based ERF by 37% and highlights the importance of historical changes in CH_4 emissions in the PD forcing of climate. It also emphasizes the potential role of CH_4 in mitigating the near-term rate of climate change (Abernethy et al., 2021; Allen et al., 2018).

4. Conclusions and Discussion

The PI-to-PD change in methane (CH_4) concentration from 808 to 1,831 ppb leads to a global mean ERF of 0.97 ± 0.04 W m^{-2} (O'Connor et al., 2021), with the majority of the forcing in the CS longwave (LW) component. Of this forcing, the direct concentration-based CH_4 contribution is 0.54 ± 0.04 W m^{-2} and is consistent with line by line radiative transfer calculations (Etminan et al., 2016) and is better represented in UKESM1 than in its predecessor model, HadGEM2. It is also consistent with the direct ERF estimate of 0.54 [0.43–0.65] W m^{-2} for 1750−2019 in the 6th assessment report (AR6) of the IPCC (Forster et al., 2021). An indirect O_3 ERF of 0.13 ± 0.05 W m^{-2} from the Elimination Method and 0.20 ± 0.04 W m^{-2} from the Single-Forcing Method is attributable to the CH_4 concentration increase, which is largely due to the tropospheric O_3 increase despite significant O_3 decreases in the stratosphere. The production of WV due to changes in CH_4 leads to a weakly positive ERF of 0.07 ± 0.05/0.02 ± 0.04 W m^{-2} – these values are consistent with previous estimates based on the SARF metric (Hansen et al., 2005; Myhre et al., 2013), suggesting that the choice of forcing metric does not have a major impact on our understanding of the role of CH_4-driven changes in WV in climate forcing.

The PI-to-PD CH_4 increase in concentration also gives rise to a positive aerosol ERF of 0.28–0.30 W m^{-2} through aci in UKESM1. CH_4-driven changes in oxidants, particularly OH, alter the relative contributions of the different sulfur dioxide (SO_2) oxidation pathways, leading to a reduction in new particle formation, a decrease in the number concentration of CCN and cloud droplets, with a corresponding increase in cloud droplet effective radius. However, the forcing from ari is negligible, consistent with the global mean aerosol optical depth changing by

less than 2%. This study also confirms that the strong positive cloud adjustment in UKESM1, as defined and quantified in Thornhill, Collins, Kramer, et al. (2021), is aerosol-mediated.

Previous studies have found an aerosol forcing attributable to CH_4 and/or oxidant changes. Shindell et al. (2009), for example, found a large reduction in the sulfate burden on a global scale (−11%), resulting in an increase of ∼10% (∼20–40%) in the PD 100-year global warming potential of CH_4 when chemistry-aerosol interactions and ari (ari and aci) were considered. Kurtén et al. (2011) reported a global mean decrease in CDNC of 18%, reduced cloudiness, and a strong positive aerosol forcing (2.32 W m^{-2}) in a scenario in which they applied a 10-fold increase in CH_4, the bulk of which was due to aerosol indirect effects (2.06 W m^{-2}). More recently, Karset et al. (2018) found that the magnitude of the PD aerosol forcing reduced by 19% (−1.32 to −1.07 W m^{-2}) when the PI control simulation included PI oxidants rather than PD oxidants. The different oxidants cause greater condensate production relative to the amount of aerosol formed via nucleation, resulting in a shift in the aerosol size distribution toward larger particles, leading to cloud brightening in the PI atmosphere. The findings here are qualitatively consistent with these previous studies. However, there is disagreement on the extent to which the aerosol forcing is due to ari and/or aci, which warrants further investigation.

The inclusion of chemistry-aerosol interactions with aci leads to a positive CRE in the PD CH_4 ERF from UKESM1. Although other models have a positive cloud adjustment associated with CH_4 in the AerChemMIP models (Thornhill, Collins, Kramer, et al., 2021), UKESM1 has the largest positive cloud adjustment. It was also not clear from Thornhill, Collins, Kramer, et al. (2021) why the cloud adjustments varied in both sign and magnitude (−0.06 to +0.24 W m^{-2}). This study, however, provides a process-based understanding of what is driving the positive CRE in UKESM1 and confirms that it is a combination of microphysical aci and thermodynamics adjustments. The microphysical impacts occur due to CH_4-driven changes in oxidants in UKESM1 that alter cloud activation and reflectivity, leading to a contribution to the CRE of 0.28–0.30 W m^{-2}. Although defined differently, this is consistent with the positive UKESM1 cloud adjustment from Thornhill, Collins, Kramer, et al. (2021). The thermodynamic effects are related to the radiative heating and stabilization of the upper troposphere, which on the whole reduced cloud cover and convection. This led to a negative CRE of −0.12 W m^{-2} due to a dominant negative LW CRE of −0.35 W m^{-2} and a positive SW CRE of 0.23 W m^{-2}. Overall, this means a CH_4-driven net CRE of 0.12 W m^{-2}. The cloud effects and other non-cloud forcing components added in a reasonably linear manner in our series of experiments, confirming that the assumption of linearity in radiative kernel analysis is valid.

If the contribution of aci to the CRE was robustly positive across models, the results would have wider implications for the role of CH_4 in historical and future climate and/or future climate mitigation. For example, future climate forcing and the ES response to continuing increases in anthropogenic emissions of CH_4 (e.g., Jackson et al., 2020; Saunois et al., 2020) and/or from feedbacks on natural CH_4 emissions (e.g., Dean et al., 2018; Gedney et al., 2019; O'Connor et al., 2010) would be greater than realised to date. CH_4 mitigation and CH_4 removal may be even more effective in reducing the total anthropogenic forcing on the Earth's radiative balance and the near-term climate response (e.g., Abernethy et al., 2021; Allen et al., 2021). However, the multi-model assessment of Thornhill, Collins, Kramer, et al. (2021) suggests that the cloud adjustment in UKESM1 is anomalously large with respect to the other AerChemMIP models. A number of factors could be driving this: (a) an anomalous CH_4-driven oxidant response in UKESM1, (b) the lack of alternative nucleation mechanisms in UKESM1, such as boundary layer nucleation (c) the lack of models in Thornhill, Collins, Kramer, et al. (2021), with interactive chemistry coupled to two-moment aerosol schemes, with the latter required for accurately simulating number concentrations of CCN (Bellouin et al., 2013), and/or (d) the cloud response to aerosols in UKESM1 being too strong and/or that in the other models being too weak.

In relation to the oxidant response, the CH_4-OH feedback factor (Fiore et al., 2009) from UKESM1 appears to be consistent with other models (Thornhill, Collins, Kramer, et al., 2021), suggesting that the OH response, at least, is reasonable. This is supported by the sensitivity of OH and CH_4 lifetime in UKESM1 to CH_4 being in agreement with other AerChemMIP models over the historical period (Stevenson et al., 2020) although the number of participating models was limited. While we acknowledge that other drivers can affect OH, such as nitrogen oxides (Murray et al., 2014; Nicely et al., 2018), these are less relevant in the idealized simulations analyzed here. The other key oxidant, responsible for nearly half the SO_2 oxidation in the PI atmosphere in UKESM1, is H_2O_2. With H_2O_2 being highly variable in space and time due to photochemistry and meteorology (e.g., Allen et al., 2013), a better understanding of the H_2O_2 budget is needed. With limited availability of direct observations of H_2O_2 and indirect measures of its abundance (Archibald et al., 2020), targeted model studies could aim to quantify

the sensitivity of its abundance to different factors such as nitrogen oxide and biogenic VOC concentrations (e,g, Miller & Brune, 2022), biomass burning (e.g., Allen et al., 2022), and HO_2 uptake on aerosols (e.g., Mao et al., 2010). In relation to nucleation, Gordon et al. (2016) demonstrated how the inclusion of organic-mediated boundary layer nucleation could weaken the PD aerosol forcing by nearly 30% by increasing the CDNC in the PI atmosphere to a greater extent than in the PD period. While boundary layer nucleation is not included in the UKESM1 simulations here, it has been found to improve model biases in PD aerosol number concentrations (Ranjithkumar et al., 2021). For the cloud response to aerosols, Malavelle et al. (2017) showed that aci seem to be more realistic in the HadGEM3 model (i.e., the physical model underpinning UKESM1) than in other models by evaluating the response to a large volcanic perturbation using observations of cloud properties. However, McCoy et al. (2020) show that the PD-PI change in CDNC from HadGEM3 is inconsistent with observational proxies as well as being outside of the range of AeroCom models. This could be due to insufficient representation of background natural aerosol, including a lack of representation of boundary layer nucleation or could be due to CDNC being too high in the northern hemisphere in response to anthropogenic aerosol emissions. This latter response could be related to the hygroscopicity of sulfate aerosol being too high in UKESM1 in comparison to recommendations from Petters and Kreidenweis (2007) and may be responsible for the strong positive CRE in the CH_4 ERF here and warrants further investigation. While progress has been made more generally on narrowing the uncertainty range of PD ERF estimates, considerable uncertainties remain in relation to rapid adjustments, the PI state, and process representation in ESMs, particularly aci (Forster et al., 2021; Ramaswamy et al., 2019). In the case of CH_4, for improved and robust estimates of its ERF, there is a need to include interactive chemistry coupled to two-moment aerosol schemes in ESMs followed by careful and systematic process-based evaluation. Further progress could be made by inter-comparing simulations with ESMs of comparable complexity, and by targeted process studies and observations to quantify and constrain all the relevant processes in the chemistry-aerosol-cloud coupling chain.

Nevertheless, these results from UKESM1 indicate the potential importance of including interactive chemistry coupled to two-moment aerosol schemes in ESMs when quantifying PD climate forcing. The 1850–2014 ERF from CH_4 emissions estimated here, including chemistry-aerosol-cloud interactions, is 1.33 ± 0.11 W m^{-2}. It is well within the very likely range of 0.81–1.58 W m^{-2} from AR6 (Szopa et al., 2021) for the 1750–2019 period, although the uncertainty is large. Such chemistry-aerosol-cloud interactions are relevant to forcings from other gas-phase constituents (O'Connor et al., 2021) as well as from the aerosol phase (Karset et al., 2018). The study also suggests that rapid adjustments included in the ERF framework should include chemical as well as physical adjustments to fully account for ES interactions. This is consistent with a recent assessment by Ramaswamy et al. (2019) who concluded that the radiative forcing concept is simple but needs to increasingly account for complex ES processes.

Data Availability Statement

Table 1 lists the model simulation identifiers for all model experiments presented in this study. Data from the *piClim-control* and *piClim-CH4* simulations have been published on the Earth System Grid Federation and the model source ID is UKESM1-0-LL, with data citations of https://doi.org/10.22033/ESGF/CMIP6.6276 and https://doi.org/10.22033/ESGF/CMIP6.6229, respectively. Plotting scripts and data can be found at zenodo with digital object identifier https://doi.org/10.5281/zenodo.5789528. All simulation data used in this study are also archived at the Met Office and are available for research purposes through the JASMIN platform (www.jasmin.ac.uk). For details, please contact UM_collaboration@metoffice.gov.uk referencing this paper.

Acknowledgments
The development of the UK's Earth System Model, UKESM1, was funded by the Met Office Hadley Centre Climate Programme funded by BEIS and Defra (GA01101) and by the National Environmental Research Council national capability grant for the UK Earth System Modelling project, Grant NE/N017951/1. FMO'C, TA, BTJ, and JPM were supported by the Met Office Hadley Centre Climate Programme funded by BEIS. FMO'C also acknowledges the EU Horizon 2020 Research Programme CRESCENDO (grant agreement number 641816) and ESM2025 (grant agreement number 101003536) projects.

References

Abdul-Razzak, H., & Ghan, S. J. (2000). A parameterization of aerosol activation 2. Multiple aerosol types. *Journal of Geophysical Research*, *105*(D5), 6837–6844. https://doi.org/10.1029/1999JD901161

Abernethy, S., O'Connor, F. M., Jones, C. D., & Jackson, R. B. (2021). Methane removal and the proportional reductions in surface temperature and ozone. *Philosophical Transactions of the Royal Society A*, *379*(2210), 20210104. https://doi.org/10.1098/rsta.2021.0104

Allen, H. M., Crounse, J. D., Kim, M. J., Teng, A. P., Ray, E. A., McKain, K., et al. (2022). H_2O_2 and CH_3OOH (MHP) in the remote atmosphere: 1. Global distribution and regional influences. *Journal of Geophysical Research: Atmospheres*, *127*(6), e2021JD035701. https://doi.org/10.1029/2021JD035701

Allen, M. R., Shine, K. P., Fuglestvedt, J. S., Millar, R. J., Cain, M., Frame, D. J., & Macey, A. H. (2018). A solution to the misrepresentations of CO_2-equivalent emissions of short-lived climate pollutants under ambitious mitigation. *npj Climate and Atmospheric Science*, *1*, 16. https://doi.org/10.1038/s41612-018-0026-8

Allen, N. D. C., Abad, G. G., Bernath, P. F., & Boone, C. D. (2013). Satellite observations of the global distribution of hydrogen peroxide (H_2O_2) from ACE. *Journal of Quantitative Spectroscopy and Radiative Transfer*, *115*, 66–77. https://doi.org/10.1016/j.jqsrt.2012.09.008

Allen, R. J., Horowitz, L. W., Naik, V., Oshima, N., O'Connor, F. M., Turnock, S., et al. (2021). Significant climate benefits from near-term climate forcer mitigation in spite of aerosol reductions. *Environmental Research Letters*, *16*, 034010. https://doi.org/10.1088/1748-9326/abe06b

Andrews, T. (2014). Using an AGCM to diagnose historical effective radiative forcing and mechanisms of recent decadal climate change. *Journal of Climate*, *27*(3), 1193–1209. https://doi.org/10.1175/JCLI-D-13-00336.1

Andrews, T., Smith, C. J., Myhre, G., Forster, P. M., Chadwick, R., & Ackerley, D. (2021). Effective radiative forcing in a GCM with fixed surface temperatures. *Journal of Geophysical Research: Atmospheres*, *126*(4), e2020JD033880. https://doi.org/10.1029/2020JD033880

Archibald, A. T., O'Connor, F. M., Abraham, N. L., Archer-Nicholls, S., Chipperfield, M. P., Dalvi, M., et al. (2020). Description and evaluation of the UKCA stratosphere-troposphere chemistry scheme (StratTrop vn 1.0) implemented in UKESM1. *Geoscientific Model Development*, *13*(3), 1223–1266. https://doi.org/10.5194/gmd-13-1223-2020

Arfeuille, F., Weisenstein, D., Mack, H., Rozanov, E., Peter, T., & Brönnimann, S. (2014). Volcanic forcing for climate modeling: A new microphysics-based data set covering years 1600–present. *Climate of the Past*, *10*(1), 359–375. https://doi.org/10.5194/cp-10-359-2014

Bauer, S. E., Tsigaridis, K., Faluvegi, G., Kelley, M., Lo, K. K., Miller, R. L., et al. (2020). Historical (1850–2014) aerosol evolution and role on climate forcing using the GISS ModelE2.1 contribution to CMIP6. *Journal of Advances in Modeling Earth Systems*, *12*(8), e2019MS001978. https://doi.org/10.1029/2019ms001978

Bellouin, N., Mann, G. W., Woodhouse, M. T., Johnson, C., Carslaw, K. S., & Dalvi, M. (2013). Impact of the modal aerosol scheme GLOMAP-mode on aerosol forcing in the Hadley Centre global environmental model. *Atmospheric Chemistry and Physics*, *13*(6), 3027–3044. https://doi.org/10.5194/acp-13-3027-2013

Boucher, O., Friedlingstein, P., Collins, B., & Shine, K. P. (2009). The indirect global warming potential and global temperature change potential due to methane oxidation. *Environmental Research Letters*, *4*, 044007. https://doi.org/10.1088/1748-9326/4/4/044007

Carslaw, K. S., Lee, L. A., Reddington, C. L., Pringle, K. J., Rap, A., Forster, P. M., et al. (2013). Large contribution of natural aerosols to uncertainty in indirect forcing. *Nature*, *503*(7474), 67–71. https://doi.org/10.1038/nature12674

Chung, E.-S., & Soden, B. J. (2015). An assessment of methods for computing radiative forcing in climate models. *Environmental Research Letters*, *10*(7), 074004. https://doi.org/10.1088/1748-9326/10/7/074004

Collins, W. D., Ramaswamy, V., Schwarzkopf, M. D., Sun, Y., Portmann, R. W., Fu, Q., et al. (2006). Radiative forcing by well-mixed greenhouse gases: Estimates from climate models in the intergovernmental panel on climate change (IPCC) fourth assessment report (AR4). *Journal of Geophysical Research*, *111*(D14), D14317. https://doi.org/10.1029/2005JD006713

Collins, W. J., Bellouin, N., Doutriaux-Boucher, M., Gedney, N., Halloran, P., Hinton, T., et al. (2011). Development and evaluation of an Earth-system model – HadGEM2. *Geoscientific Model Development*, *4*, 1051–1075. https://doi.org/10.5194/gmd-4-1051-2011

Collins, W. J., Lamarque, J.-F., Schulz, M., Boucher, O., Eyring, V., Hegglin, M. I., et al. (2017). AerChemMIP: Quantifying the effects of chemistry and aerosols in CMIP6. *Geoscientific Model Development*, *10*(2), 585–607. https://doi.org/10.5194/gmd-10-585-2017

Dean, J. F., Middelburg, J. J., Röckmann, T., Aerts, R., Blauw, L. G., Egger, M., et al. (2018). Methane feedbacks to the global climate system in a warmer world. *Reviews of Geophysics*, *56*(1), 207–250. https://doi.org/10.1002/2017RG000559

Dessler, A. E., Schoeberl, M. R., Wang, T., Davis, S. M., & Rosenlof, K. H. (2013). Stratospheric water vapor feedback. *Proceedings of the National Academy of Sciences*, *110*(45), 18087–18091. https://doi.org/10.1073/pnas.1310344110

Edwards, J. M., & Slingo, A. (1996). Studies with a flexible new radiation code. I: Choosing a configuration for a large-scale model. *Quarterly Journal of the Royal Meteorological Society*, *122*(531), 689–719. https://doi.org/10.1002/qj.49712253107

Emmons, L. K., Schwantes, R. H., Orlando, J. J., Tyndall, G., Kinnison, D., Marsh, D., et al. (2020). The chemistry mechanism in the community Earth system model version 2 (CESM2). *Journal of Advances in Modeling Earth Systems*, *12*(4). https://doi.org/10.1029/2019MS001882

Etminan, M., Myhre, G., Highwood, E. J., & Shine, K. P. (2016). Radiative forcing of carbon dioxide, methane, and nitrous oxide: A significant revision of the methane radiative forcing. *Geophysical Research Letters*, *43*(24), 12614–12623. https://doi.org/10.1002/2016GL071930

Eyring, V., Bony, S., Meehl, G. A., Senior, C. A., Stevens, B., Stouffer, R. J., & Taylor, K. E. (2016). Overview of the coupled model Intercomparison project phase 6 (CMIP6) experimental design and organization. *Geoscientific Model Development*, *9*(5), 1937–1958. https://doi.org/10.5194/gmd-9-1937-2016

Fiore, A. M., Dentener, F. J., Wild, O., Cuvelier, C., Schultz, M. G., Hess, P., et al. (2009). Multimodel estimates of intercontinental source-receptor relationships for ozone pollution. *Journal of Geophysical Research: Atmospheres*, *114*(D4), D04301. https://doi.org/10.1029/2008JD010816

Folberth, G. A., Staniaszek, Z., Archibald, A. T., Gedney, N., Griffiths, P. T., Jones, C. D., et al. (2022). Description and evaluation of an emission-driven and fully coupled methane cycle in UKESM1. *Journal of Advances in Modeling Earth Systems*, *14*(7), e2021MS002982. https://doi.org/10.1029/2021MS002982

Forster, P., Ramaswamy, V., Artaxo, P., Berntsen, T., Betts, R., Fahey, D. W., et al. (2007). Changes in atmospheric constituents and in radiative forcing. In S. Solomon, D. Qin, M. Manning, Z. Chen, M. Marquis, K. B. Averyt, et al. (Eds.), *Climate change 2007: The physical science basis. Contribution of working group I to the fourth assessment report of the intergovernmental panel on climate change*. Cambridge University Press.

Forster, P., Storelvmo, T., Armour, K., Collins, W., Dufresne, J.-L., Frame, D., et al. (2021). The Earth's energy budget, climate feedbacks, and climate sensitivity. In P. Zhai, A. Pirani, S. L. Connors, C. Péan, S. Berger, N. Caud, et al. (Eds.), *Climate change 2021: The physical science basis. Contribution of working group I to the sixth assessment report of the intergovernmental panel on climate change Masson-Delmotte, V* (pp. 923–1054). Cambridge University Press. https://doi.org/10.1017/9781009157896.009

Forster, P. M., Richardson, T., Maycock, A. C., Smith, C. J., Samset, B. H., Myhre, G., et al. (2016). Recommendations for diagnosing effective radiative forcing from climate models for CMIP6. *Journal of Geophysical Research: Atmospheres*, *121*(20), 12460–12475. https://doi.org/10.1002/2016JD025320

Forster, P. M., & Shine, K. P. (1999). Stratospheric water vapour changes as a possible contributor to observed stratospheric cooling. *Geophysical Research Letters*, *26*(21), 3309–3312. https://doi.org/10.1029/1999GL010487

Forster, P. M. F., & Shine, K. P. (2002). Assessing the climate impact of trends in stratospheric water vapor. *Geophysical Research Letters*, *29*(6). https://doi.org/10.1029/2001GL013909

Gedney, N., Huntingford, C., Comyn-Platt, E., & Wiltshire, A. (2019). Significant feedbacks of wetland methane release on climate change and the causes of their uncertainty. *Environmental Research Letters*, *14*(8), 084027. https://doi.org/10.1088/1748-9326/ab2726

Ghan, S. J. (2013). Technical Note: Estimating aerosol effects on cloud radiative forcing. *Atmospheric Chemistry and Physics*, *13*(19), 9971–9974. https://doi.org/10.5194/acp-13-9971-2013

Ghan, S. J., Liu, X., Easter, R. C., Zaveri, R., Rasch, P. J., Yoon, J., & Eaton, B. (2012). Toward a minimal representation of aerosols in climate models: Comparative decomposition of aerosol direct, semidirect, and indirect radiative forcing. *Journal of Climate*, *25*(19), 6461–6476. https://doi.org/10.1175/JCLI-D-11-00650.1

Gordon, H., Sengupta, K., Rap, A., Duplissy, J., Frege, C., Williamson, C., et al. (2016). Biogenic particle formation and aerosol forcing. *Proceedings of the National Academy of Sciences*, *113*(43), 12053–12058. https://doi.org/10.1073/pnas.1602360113

Hansen, J., Sato, M., Ruedy, R., Nazarenko, L., Lacis, A., Schmidt, G. A., et al. (2005). Efficacy of climate forcings. *Journal of Geophysical Research*, *110*(D18), D18104. https://doi.org/10.1029/2005JD005776

Hoesly, R. M., Smith, S. J., Feng, L., Klimont, Z., Janssens-Maenhout, G., Pitkanen, T., et al. (2018). Historical (1750–2014) anthropogenic emissions of reactive gases and aerosols from the Community Emissions Data System (CEDS). *Geoscientific Model Development*, *11*(1), 369–408. https://doi.org/10.5194/gmd-11-369-2018

Hsu, J., & Prather, M. J. (2010). Global long-lived chemical modes excited in a 3-D chemistry transport model: Stratospheric N_2O, NOy, O_3 and CH_4 chemistry. *Geophysical Research Letters*, *37*(7), L07805. https://doi.org/10.1029/2009GL042243

Hurst, D. F., Oltmans, S. J., Vömel, H., Rosenlof, K. H., Davis, S. M., Ray, E. A., et al. (2011). Stratospheric water vapor trends over Boulder, Colorado: Analysis of the 30 year Boulder record. *Journal of Geophysical Research*, *116*(D2), D02306. https://doi.org/10.1029/2010JD015065

Iglesias-Suarez, F., Kinnison, D. E., Rap, A., Maycock, A. C., Wild, O., & Young, P. J. (2018). Key drivers of ozone change and its radiative forcing over the 21st century. *Atmospheric Chemistry and Physics*, *18*(9), 6121–6139. https://doi.org/10.5194/acp-18-6121-2018

Jackson, R. B., Saunois, M., Bousquet, P., Canadell, J. G., Poulter, B., Stavert, A. R., et al. (2020). Increasing anthropogenic methane emissions arise equally from agricultural and fossil fuel sources. *Environmental Research Letters*, *15*(7), 071002. https://doi.org/10.1088/1748-9326/ab9ed2

Karset, I. H. H., Berntsen, T. K., Storelvmo, T., Alterskjæ, K., Grini, A., Olivié, D., et al. (2018). Strong impacts on aerosol indirect effects from historical oxidant changes. *Atmospheric Chemistry and Physics*, *18*(10), 7669–7690. https://doi.org/10.5194/acp-18-7669-2018

Kelly, J., Doherty, R. M., O'Connor, F. M., & Mann, G. W. (2018). The impact of biogenic, anthropogenic, and biomass burning emissions on regional and seasonal variations in secondary organic aerosol concentrations. *Atmospheric Chemistry and Physics*, *18*(10), 7393–7422. https://doi.org/10.5194/acp-18-7393-2018

Kleinen, T., Gromov, S., Steil, B., & Brovkin, V. (2021). Atmospheric methane underestimated in future climate projections. *Environmental Research Letters*, *16*(9), 094006. https://doi.org/10.1088/1748-9326/ac1814

Kleinen, T., Mikolajewicz, U., & Brovkin, V. (2020). Terrestrial methane emissions from the Last Glacial Maximum to the preindustrial period. *Climate of the Past*, *16*(2), 575–595. https://doi.org/10.5194/cp-16-575-2020

Kurtén, T., Zhou, L., Makkonen, R., Merikanto, J., Räisänen, P., Boy, M., et al. (2011). Large methane releases lead to strong aerosol forcing and reduced cloudiness. *Atmospheric Chemistry and Physics*, *11*(14), 6961–6969. https://doi.org/10.5194/acp-11-6961-2011

Lacis, A. A., Wuebbles, D. J., & Logan, J. A. (1990). Radiative forcing of climate by changes in the vertical distribution of ozone. *Journal of Geophysical Research*, *95*(D7), 9971–9981. https://doi.org/10.1029/jd095id07p09971

Li, J., Curry, C. L., Sun, Z., & Zhang, F. (2010). Overlap of solar and infrared spectra and the shortwave radiative effect of methane. *Journal of the Atmospheric Sciences*, *67*(7), 2372–2389. https://doi.org/10.1175/2010jas3282.1

Malavelle, F. F., Haywood, J. M., Jones, A., Gettelman, A., Clarisse, L., Bauduin, S., et al. (2017). Strong constraints on aerosol-cloud interactions from volcanic eruptions. *Nature*, *546*(7659), 485–491. (Erratum in: Nature, PMID: 28640263, 2017). https://doi.org/10.1038/nature22974

Mann, G. W., Carslaw, K. S., Spracklen, D. V., Ridley, D. A., Manktelow, P. T., Chipperfield, M. P., et al. (2010). Description and evaluation of GLOMAP-mode: A modal global aerosol microphysics model for the UKCA composition-climate model. *Geoscientific Model Development*, *3*(2), 519–551. https://doi.org/10.5194/gmd-3-519-2010

Mao, J., Jacob, D. J., Evans, M. J., Olson, J. R., Ren, X., Brune, W. H., et al. (2010). Chemistry of hydrogen oxide radicals (HOx) in the Arctic troposphere in spring. *Atmospheric Chemistry and Physics*, *10*(13), 5823–5838. https://doi.org/10.5194/acp-10-5823-2010

Matthes, K., Funke, B., Andersson, M. E., Barnard, L., Beer, J., Charbonneau, P., et al. (2017). Solar forcing for CMIP6 (v3.2). *Geoscientific Model Development*, *10*(6), 2247–2302. https://doi.org/10.5194/gmd-10-2247-2017

McCoy, I. L., McCoy, D. T., Wood, R., Regayre, L., Watson-Parris, D., Grosvenor, D. P., et al. (2020). The hemispheric contrast in cloud microphysical properties constrains aerosol forcing. *Proceedings of the National Academy of Sciences*, *117*(32), 18998–19006. https://doi.org/10.1073/pnas.1922502117

Meinshausen, M., Vogel, E., Nauels, A., Lorbacher, K., Meinshausen, N., Etheridge, D. M., et al. (2017). Historical greenhouse gas concentrations for climate modelling (CMIP6). *Geoscientific Model Development*, *10*(5), 2057–2116. https://doi.org/10.5194/gmd-10-2057-2017

Miller, D. O., & Brune, W. H. (2022). Investigating the understanding of oxidation chemistry using 20 years of airborne OH and HO_2 observations. *Journal of Geophysical Research: Atmospheres*, *127*(1), e2021JD035368. https://doi.org/10.1029/2021JD035368

Morgenstern, O., Braesicke, P., O'Connor, F. M., Bushell, A. C., Johnson, C. E., Osprey, S. M., & Pyle, J. A. (2009). Evaluation of the new UKCA climate-composition model – Part 1: The stratosphere. *Geoscientific Model Development*, *2*, 43–57. https://doi.org/10.5194/gmd-2-43-2009

Morgenstern, O., Hegglin, M. I., Rozanov, E., O'Connor, F. M., Abraham, N. L., Akiyoshi, H., et al. (2017). Review of the global models used within phase 1 of the chemistry–climate model initiative (CCMI). *Geoscientific Model Development*, *10*(2), 639–671. https://doi.org/10.5194/gmd-10-639-2017

Mulcahy, J. P., Johnson, C., Jones, C. G., Povey, A. C., Scott, C. E., Sellar, A., et al. (2020). Description and evaluation of aerosol in UKESM1 and HadGEM3-GC3.1 CMIP6 historical simulations. *Geoscientific Model Development*, *13*(12), 6383–6423. https://doi.org/10.5194/gmd-13-6383-2020

Mulcahy, J. P., Jones, C., Sellar, A., Johnson, B., Boutle, I. A., Jones, A., et al. (2018). Improved aerosol processes and effective radiative forcing in HadGEM3 and UKESM1. *Journal of Advances in Modeling Earth Systems*, *10*(11), 2786–2805. https://doi.org/10.1029/2018MS001464

Murray, L. T., Mickley, L. J., Kaplan, J. O., Sofen, E. D., Pfeiffer, M., & Alexander, B. (2014). Factors controlling variability in the oxidative capacity of the troposphere since the Last Glacial Maximum. *Atmospheric Chemistry and Physics*, *14*(7), 3589–3622. https://doi.org/10.5194/acp-14-3589-2014

Myhre, G., Nilsen, J., Gulstad, L., Shine, K., Rognerud, B., & Isaksen, I. (2007). Radiative forcing due to stratospheric water vapour from CH_4 oxidation. *Geophysical Research Letters*, *34*(1), L01807. https://doi.org/10.1029/2006GL027472

Myhre, G., Shindell, D., Bréon, F.-M., Collins, W., Fuglestvedt, J., Huang, J., et al. (2013). Anthropogenic and natural radiative forcing. In T. F. Stocker, D. Qin, G.-K. Plattner, M. Tignor, S. K. Allen, J. Boschung, et al. (Eds.), *Climate change 2013: The physical science basis. Contribution of working group I to the fifth assessment report of the intergovernmental Panel on climate change*. Cambridge University Press.

Nicely, J. M., Canty, T. P., Manyin, M., Oman, L. D., Salawitch, R. J., Steenrod, S. D., et al. (2018). Changes in global tropospheric OH expected as a result of climate change over the last several decades. *Journal of Geophysical Research: Atmospheres*, *123*(18), 10774–10795. https://doi.org/10.1029/2018JD028388

Ocko, I. B., Naik, V., & Paynter, D. (2018). Rapid and reliable assessment of methane impacts on climate. *Atmospheric Chemistry and Physics*, *18*(21), 15555–15568. https://doi.org/10.5194/acp-18-15555-2018

O'Connor, F. (2019a). MOHC UKESM1.0-LL model output prepared for CMIP6 AerChemMIP piClim-control (Version 20211115). Earth System Grid Federation. https://doi.org/10.22033/ESGF/CMIP6.6276

O'Connor, F. (2019b). MOHC UKESM1.0-LL model output prepared for CMIP6 AerChemMIP piClim-CH4 (Version 20211115). Earth System Grid Federation. https://doi.org/10.22033/ESGF/CMIP6.6229

O'Connor, F. M., Abraham, N. L., Dalvi, M., Folberth, G., Griffiths, P., Hardacre, C., et al. (2021). Assessment of pre-industrial to present-day anthropogenic climate forcing in UKESM1. *Atmospheric Chemistry and Physics*, *21*(2), 1211–1243. https://doi.org/10.5194/acp-21-1211-2021

O'Connor, F. M., Boucher, O., Gedney, N., Jones, C. D., Folberth, G. A., Coppell, R., et al. (2010). The possible role of wetlands, permafrost and methane hydrates in the future methane cycle: A review. *Reviews of Geophysics*, *48*(4), RG4005. https://doi.org/10.1029/2010RG000326

O'Connor, F. M., Johnson, C. E., Morgenstern, O., Abraham, N. L., Braesicke, P., Dalvi, M., et al. (2014). Evaluation of the new UKCA climate-composition model. Part II. The troposphere. *Geoscientific Model Development*, *7*(1), 41–91. https://doi.org/10.5194/gmd-7-41-2014

Oman, L., Waugh, D. W., Pawson, S., Stolarski, R. S., & Nielsen, J. E. (2011). Understanding the changes of stratospheric water vapor in coupled chemistry–climate model simulations. *Journal of the Atmospheric Sciences*, *65*(10), 3278–3291. https://doi.org/10.1175/2008JAS2696.1

Pawson, S., Steinbrecht, W., Charlton-Perez, A. J., Fujiwara, M., Karpechko, A. Y., Petropavlovskikh, I., et al. (2014). Update on global ozone: Past, present, and future. In *Chapter 2 in scientific assessment of ozone depletion: 2014, global ozone research and monitoring project – report No. 55*. World Meteorological Organization.

Petters, M. D., & Kreidenweis, S. M. (2007). A single parameter representation of hygroscopic growth and cloud condensation nucleus activity. *Atmospheric Chemistry and Physics*, *7*(8), 1961–1971. https://doi.org/10.5194/acp-7-1961-2007

Pincus, R., Buehler, S. A., Brath, M., Crevoisier, C., Jamil, O., Evans, K. F., et al. (2020). Benchmark calculations of radiative forcing by greenhouse gases. *Journal of Geophysical Research: Atmospheres*, *125*(23), e2020JD033483. https://doi.org/10.1029/2020JD033483

Pincus, R., Forster, P. M., & Stevens, B. (2016). The radiative forcing model Intercomparison project (RFMIP): Experimental protocol for CMIP6. *Geoscientific Model Development*, *9*, 3447–3460. https://doi.org/10.5194/gmd-9-3447-2016

Prather, M., Holmes, C., & Hsu, J. (2012). Reactive greenhouse gas scenarios: Systematic exploration of uncertainties and the role of atmospheric chemistry. *Geophysical Research Letters*, *39*(9). https://doi.org/10.1029/2012GL051440

Prather, M. J., Ehhalt, D., Dentener, F., Derwent, R., Dlugokencky, E., Holland, E., et al. (2001). Atmospheric chemistry and greenhouse gases. In J. T. Houghton, Y. Ding, D. J. Griggs, M. Noguer, P. J. van der Linden, X. Dai, et al. (Eds.), *Climate change 2001: The scientific basis. Contribution of working group I to the third assessment report of the intergovernmental Panel on climate change*. Cambridge University Press.

Ramaswamy, V., Boucher, O., Haigh, J., Hauglustaine, D., Haywood, J., Myhre, G., et al. (2001). Radiative forcing of climate change (Eds.). In *Climate change 2001: The scientific basis. Contribution of working group I to the third assessment report of the intergovernmental Panel on climate change*. Cambridge Univ. Press.

Ramaswamy, V., Collins, W., Haywood, J., Lean, J., Mahowald, N., Myhre, G., et al. (2019). Radiative forcing of climate: The historical evolution of the radiative forcing concept, the forcing agents and their quantification, and applications. *American Meteorol. Soc. Centenary Monograph*, *1*. https://doi.org/10.1175/AMSMONOGRAPHS-D-19-0001

Ranjithkumar, A., Gordon, H., Williamson, C., Rollins, A., Pringle, K., Kupc, A., et al. (2021). Constraints on global aerosol number concentration, SO_2 and condensation sink in UKESM1 using ATom measurements. *Atmospheric Chemistry and Physics*, *21*(6), 4979–5014. https://doi.org/10.5194/acp-21-4979-2021

Richardson, T. B., Forster, P. M., Smith, C. J., Maycock, A. C., Wood, T., Andrews, T., et al. (2019). Efficacy of climate forcings in PDRMIP models. *Journal of Geophysical Research: Atmospheres*, *124*(23), 12824–12844. https://doi.org/10.1029/2019JD030581

Saunois, M., Stavert, A. R., Poulter, B., Bousquet, P., Canadell, J. G., Jackson, R. B., et al. (2020). The global methane budget 2000-2017. *Earth System Science Data*, *12*(3), 1–63. https://doi.org/10.5194/essd-12-1561-2020

Sellar, A. A., Jones, C. G., Mulcahy, J., Tang, Y., Yool, A., Wiltshire, A., et al. (2019). UKESM1: Description and evaluation of the UK Earth system model. *Journal of Advances in Modeling Earth Systems*, *11*(12), 4513–4558. https://doi.org/10.1029/2019MS001739

Shindell, D., Faluvegi, G., Nazarenko, L., Bowman, K., Lamarque, J.-F., Voulgarakis, A., et al. (2013). Attribution of historical ozone forcing to anthropogenic emissions. *Nature Climate Change*, *3*(6), 567–570. https://doi.org/10.1038/nclimate1835

Shindell, D. T., Faluvegi, G., Bell, N., & Schmidt, G. A. (2005). An emissions-based view of climate forcing by methane and tropospheric ozone. *Geophysical Research Letters*, *32*(4), L04803. https://doi.org/10.1029/2004GL021900

Shindell, D. T., Faluvegi, G., Koch, D. M., Schmidt, G. A., Unger, N., & Bauer, S. E. (2009). Improved attribution of climate forcing to emissions. *Science*, *326*(5953), 716–718. https://doi.org/10.1126/science.1174760

Skeie, R. B., Myhre, G., Hodnebrog, Ø., Cameron-Smith, P. J., Deushi, M., Hegglin, M. I., et al. (2020). Historical total ozone radiative forcing derived from CMIP6 simulations. *Npj Climate and Atmospheric Science*, *3*(1), 32. https://doi.org/10.1038/s41612-020-00131-0

Smith, C. J., Kramer, R. J., Myhre, G., Alterskjær, K., Collins, W., Sima, A., et al. (2020). Effective radiative forcing and adjustments in CMIP6 models. *Atmospheric Chemistry and Physics*, *20*(16), 9591–9618. https://doi.org/10.5194/acp-20-9591-2020

Smith, C. J., Kramer, R. J., Myhre, G., Forster, P. M., Soden, B. J., Andrews, T., et al. (2018). Understanding rapid adjustments to diverse forcing agents. *Geophysical Research Letters*, *45*(21), 12023–12031. https://doi.org/10.1029/2018GL079826

Stenke, A., & Grewe, V. (2005). Simulation of stratospheric water vapor trends: Impact on stratospheric ozone chemistry. *Atmospheric Chemistry and Physics*, *5*, 1257–1272. https://doi.org/10.5194/acp-5-1257-2005

Stevenson, D. S., Zhao, A., Naik, V., O'Connor, F. M., Tilmes, S., Zeng, G., et al. (2020). Trends in global tropospheric hydroxyl radical and methane lifetime since 1850 from AerChemMIP. *Atmospheric Chemistry and Physics*, *20*(21), 12905–12920. https://doi.org/10.5194/acp-20-12905-2020

Szopa, S., Naik, V., Adhikary, B., Artaxo, P., Berntsen, T., Collins, W. D., et al. (2021). Short-Lived climate forcers. In P. Zhai, A. Pirani, S. L. Connors, C. Péan, S. Berger, N. Caud, et al. (Eds.), *Climate change 2021: The physical science basis. Contribution of working group I to the sixth assessment report of the intergovernmental Panel on climate change [Masson-Delmotte, V* (pp. 817–922). Cambridge University Press. https://doi.org/10.1017/9781009157896.008

Thomason, L. W., Ernest, N., Millán, L., Rieger, L., Bourassa, A., Vernier, J.-P., et al. (2018). A global space-based stratospheric aerosol climatology: 1979–2016. *Earth System Science Data*, *10*(1), 469–492. https://doi.org/10.5194/essd-10-469-2018

Thornhill, G. D., Collins, W., Olivié, D., Skeie, R. B., Archibald, A., Bauer, S., et al. (2021). Climate-driven chemistry and aerosol feedbacks in CMIP6 Earth system models. *Atmospheric Chemistry and Physics*, *21*(2), 1105–1126. https://doi.org/10.5194/acp-21-1105-2021

Thornhill, G. D., Collins, W. J., Kramer, R. J., Olivié, D., Skeie, R. B., O'Connor, F. M., et al. (2021). Effective radiative forcing from emissions of reactive gases and aerosols – A multi-model comparison. *Atmospheric Chemistry and Physics*, *21*(2), 853–874. https://doi.org/10.5194/acp-21-853-2021

Turnock, S. T., Mann, G. W., Woodhouse, M. T., Dalvi, M., O'Connor, F. M., Carslaw, K. S., & Spracklen, D. V. (2019). The impact of changes in cloud water pH on aerosol radiative forcing. *Geophysical Research Letters*, *46*(7), 4039–4048. https://doi.org/10.1029/2019GL082067

Twomey, S. (1977). The influence of pollution on the shortwave albedo of clouds. *Journal of the Atmospheric Sciences*, *34*(7), 1149–1152. https://doi.org/10.1175/1520-0469(1977)034<1149:TIOPOT>2.0.CO;2

United Nations Environment Programme and Climate and Clean Air Coalition. (2021). *Global methane assessment: Benefits and costs of mitigating methane emissions*. United Nations Environment Programme.

United Nations Environment Programme (UNEP) and World Meteorological Organization (WMO). (2011). Integrated assessment of black carbon and tropospheric ozone. Retrieved from https://wedocs.unep.org/20.500.11822/8028

van Marle, M. J. E., Kloster, S., Magi, B. I., Marlon, J. R., Daniau, A.-L., Field, R. D., et al. (2017). Historic global biomass burning emissions for CMIP6 (BB4CMIP) based on merging satellite observations with proxies and fire models (1750–2015). *Geoscientific Model Development*, *10*(9), 3329–3357. https://doi.org/10.5194/gmd-10-3329-2017

Vehkamäki, H., Kulmala, M., Napari, I., Lehtinen, K. E. J., Timmreck, C., Noppel, M., & Laaksonen, A. (2002). An improved parameterization for sulfuric acid–water nucleation rates for tropospheric and stratospheric conditions. *Journal of Geophysical Research: Atmospheres*, *107*(D22), AAC3–1–AAC3–10. https://doi.org/10.1029/2002JD002184

Walters, D., Baran, A. J., Boutle, I., Brooks, M., Earnshaw, P., Edwards, J., et al. (2019). The Met Office unified model global atmosphere 7.0/7.1 and JULES global land 7.0 configurations. *Geoscientific Model Development*, *12*(5), 1909–1963. https://doi.org/10.5194/gmd-12-1909-2019

Wilcox, L. J., Shine, K. P., & Hoskins, B. J. (2012). Radiative forcing due to aviation water vapour emissions. *Atmospheric Environment*, *63*, 1–13. https://doi.org/10.1016/j.atmosenv.2012.08.072

Winterstein, F., Tanalski, F., Jöckel, P., Dameris, M., & Ponater, M. (2019). Implication of strongly increased atmospheric methane concentrations for chemistry–climate connections. *Atmospheric Chemistry and Physics*, *19*(10), 7151–7163. https://doi.org/10.5194/acp-19-7151-2019

Zelinka, M. D., Andrews, T., Forster, P. M., & Taylor, K. E. (2014). Quantifying components of aerosol-cloud-radiation interactions in climate models. *Journal of Geophysical Research: Atmospheres*, *119*(12), 7599–7615. https://doi.org/10.1002/2014JD021710